Bulletin of Engineering Geology and the Environment (2024) 83:107
https://doi.org/10.1007/s10064-024-03602-3

ORIGINAL PAPER

Three-dimensional stability analysis of tunnel face considering the upper partial failure in layered rock masses

Guang-Hui Chen[1,2] · **Jin-Feng Zou**[2]

Received: 16 August 2022 / Accepted: 2 March 2024 / Published online: 12 March 2024

Abstract
The aim of this study is to assess the three-dimensional (3D) stability of the tunnel face with considering the possibility of the upper partial failure in layered rock masses. The failure characteristic of the rock material is denoted by the nonlinear Hoek–Brown failure criterion, and a multi-tangent method is introduced and adopted to determine the equivalent Mohr–Coulomb parameters. Based on the traditional 3D rotational failure model, the whole failure model and the upper partial failure model are developed with considering layered rock masses and possibility of upper partial failure at the tunnel face. The upper-bound limit analysis approach is adopted to determine the limit support pressure and failure surface. The proposed method is validated by comparison with existing solutions and numerical results. Parametrical analysis is then conducted to investigate the influence of analytical parameters on the face stability. Finally, the effect of seepage forces on the tunnel face stability is presented. The results show that, the upper partial failure is likely to happen when a soft layer in the upper section of tunnel face. This possibility increases as properties of lower layer increase, the tunnel diameter decreases, and the layered position moves down. The presence of underground water delays the occurrence of upper partial failure at the tunnel face.

Keywords Upper partial failure · Layered rock masses · Multi-Tangent method · Upper-bound limit analysis approach · Limit support pressure · Failure surface

Introduction

In the construction of shield tunnels, the estimation of the limit support pressure is regarded as the most significant issue to assess the tunnel face stability (Hou et al. 2022; Zhang et al. 2022). This is because the lack of sufficient supporting pressures to balance the earth pressures, and the underground water pressures will result in the collapse failure of the tunnel face (Yin et al. 2021; Man et al. 2022a; Di et al. 2023a), which will then cause a large number of casualties, property losses, and delay of the construction period (Wang et al. 2019; Man et al. 2022a; Meng et al. 2022). The conventional methods to determine the limit support pressure include experimental tests (Lü et al. 2018; Weng et al. 2020; Di et al. 2023b), numerical simulations (Alagha and Chapman 2019; Wang et al. 2022), and analytical approaches (Hou et al. 2022; Zhang et al. 2022; Liu et al. 2022; Jin et al. 2021; Ding et al. 2019; Di et al. 2023c; Han et al. 2021; Jafari and Fahimifar 2022; Wu et al. 2021). Since analytical approaches can offer a meaningful physical insight into the governing parameters and provide a direct design for tunnel engineers with less time-consuming (Zou et al. 2019a; Li et al. 2022; Chen et al. 2022), analytical approaches, especially the upper-bound limit analysis approach, have been widely adopted to study the tunnel face stability issues in recent years (Hou et al. 2022; Zou et al. 2019a; Liu et al. 2021; Chen et al. 2021; Zhou and Qin 2022).

To analyze the tunnel face stability using the upper-bound limit analysis approach, a large number of analytical failure models have been proposed in recent decades (Liu et al. 2021; Zhang et al. 2015; Mollon et al. 2011; Ibrahim et al. 2015; Zou et al. 2019a; Ding et al. 2019; Di et al. 2023c), such as the two-dimensional (2D) log-spiral failure model (Liu et al. 2021), the 3D multi-block failure model (Zhang et al. 2015), and the 3D rotational failure model (Mollon et al. 2011). Among them, the 3D rotational failure model is regarded as the most popular one due to following two

✉ Guang-Hui Chen
15700731178@163.com

[1] School of Civil Engineering, Zhengzhou University, Zhengzhou, Henan 450001, People's Republic of China

[2] School of Civil Engineering, Central South University, Changsha, Hunan 410075, People's Republic of China

advantages: (1) the whole tunnel face is considered in the failure model; (2) the discretization and "point by point" techniques are employed in the generation of the failure surface by following the normality condition, which makes it possible to incorporate the layered materials into the stability assessment of tunnel faces. Since Mollon et al. (2011), the 3D rotational failure model has been extensively adopted to investigate the tunnel face stability (Ibrahim et al. 2015; Pan and Dias 2016a, 2016b; Zou et al. 2019b; Qian et al. 2019; Chen et al. 2021; Di et al. 2023c). For example, based on the 3D rotational failure model, Ibrahim et al. (2015) and Pan and Dias (2016a) respectively analyzed the effects of heterogeneous and anisotropic soils on the tunnel face stability; Pan and Dias (2016b), Zou et al. (2019b), and Di et al. (2023c) analyzed the effect of seepage forces on the tunnel face stability with the aid of numerical simulations; Qian et al. (2019) and Chen et al. (2021) respectively analyzed the effect of umbrella pipes and bolts on the tunnel face stability. It is worth noting that these published literatures are all limit to the soil materials following the linear Mohr–Coulomb yield criterion. However, in recent years, more and more rock tunnels are being constructed using the conventional mining method (Pan and Dias 2018; Seghateh Mojtahedi et al. 2021). Some studies have showed that the linear Mohr–Coulomb yield criterion is intractable for assessing the face stability of tunnels excavated in rock masses (Man et al. 2022a; Seghateh Mojtahedi et al. 2021).

To solve this problem, some researches have attempted to assess the stability of tunnel faces excavated in rock masses using the nonlinear Hoek–Brown failure criterion (Pan and Dias 2018; Seghateh Mojtahedi et al. 2021; Senent et al. 2013; Saada et al. 2013). These researches showed that the Hoek–Brown failure criterion can be effectively adopted to describe the failure characteristic of rock masses in front of the tunnel face (Pan and Dias 2018; Seghateh Mojtahedi et al. 2021). But these researches are all limit to the homogeneous rock masses. However, in practical engineering, the soil or rock masses are always layered due to the influence of environmental factors (Ibrahim et al. 2015; Man et al. 2022a). The effects of layered soils on the tunnel face stability have been studied by Ibrahim et al. (2015) and Pan and Dias (2016a). These works showed that neglecting the non-homogeneities of soil properties will result in inaccurate estimations for the stability issues of the tunnel face. But few attempts have been conducted to analyze the influence of layered rock masses on the stability of tunnel faces, except Man et al. (2022a, 2022b), in which the 2D log-spiral failure model is employed to investigate the impact of layered rock masses on the tunnel face stability. However, the practical collapse of the tunnel face is 3D failure, and the 2D failure model will inevitably result in conservative evaluations of the stability issue (Mollon et al. 2011). Furthermore, some published literatures showed that the upper partial failure is more likely to happen within the tunnel face in layered materials (Cheng et al. 2019; Senent and Jimenez 2015). But in Man et al. (2022a, 2022b), only the whole failure at the tunnel face is considered for all cases. To authors' knowledge, no attentions have been put into the analysis of the tunnel face stability with considering the possibility of upper partial failure in layered rock masses. This study will fill this research gap.

Based on the discussions above, this study aims to propose an effective approach to estimate the stability of shield tunnel faces in layered rock masses. The equivalent Mohr–Coulomb parameters of layered rock masses are derived using the multi-tangent method. Based on the traditional rotational failure model, the whole failure model and the upper partial failure model are developed with considering layered rock masses and possibility of upper partial failure at the tunnel face. Based on the upper-bound limit analysis approach, the limit support pressure is determined by maximizing the calculated results from these two failure models with the aid of the genetic algorithm. The proposed method is validated by comparisons with existing analytical solutions and numerical results. Then, parametric analysis is conducted to investigate the influence of analytical parameters on the tunnel face stability. Finally, the effect of seepage forces on the tunnel face stability is presented.

Nonlinear failure criterion and equivalent Mohr–Coulomb parameters

Because of various discontinuities with different sizes and orientations in rock masses, nearly all rock materials show the nonlinear failure characteristics at failure states (Shen et al. 2012; Zhao et al. 2017). This indicates that the traditional linear Mohr–Coulomb yield criterion cannot be used to describe the failure of rock masses (Pan and Dias 2018; Seghateh Mojtahedi et al. 2021; Zhang et al. 2019). To solve this shortcoming, in this study, the generalized nonlinear Hoek–Brown failure criterion proposed by Hoek et al. (2002) is adopted to determine the tunnel face stability in layered rock masses. In the following subsections, the generalized nonlinear Hoek–Brown failure criterion is first introduced, and then a multi-tangent method is introduced and adopted to determine the equivalent Mohr–Coulomb parameters of rock masses.

Generalized nonlinear Hoek–Brown failure criterion

The generalized nonlinear Hoek–Brown failure criterion can be expressed as (Hoek et al. 2002),

$$\sigma_1 = \sigma_3 + \sigma_{ci}\left(m_b\frac{\sigma_3}{\sigma_1} + s\right)^a \tag{1}$$

where σ_1 is the maximum effective principal stress; σ_3 is the minimum effective principal stress; σ_{ci} is the uniaxial compressive stress of the intact rock. s, a, and m_b can be calculated by following equations.

$$m_b = m_i \exp\left(\frac{GSI - 100}{28 - 14D_i}\right) \tag{2}$$

$$s = \exp\left(\frac{GSI - 100}{9 - 3D_i}\right) \tag{3}$$

$$a = \frac{1}{2} + \frac{1}{6}\left[\exp\left(-\frac{GSI}{15}\right) - \exp\left(-\frac{20}{3}\right)\right] \tag{4}$$

where m_i is the Hoek–Brown constant; GSI is the geological strength index; D_i is the disturbance factor of the intact rock. Hence, for the generalized Hoek–Brown failure criterion, there are total four input parameters, namely σ_{ci}, GSI, m_i, and D_i.

Equivalent Mohr–Coulomb parameters using the Multi-Tangent method

To incorporate the Hoek–Brown failure criterion into the stability analysis of engineering structures, the common methods are to calculate the corresponding equivalent Mohr–Coulomb parameters of rock masses by using the direct equivalent technique or the tangent method (Yang et al. 2004; Pan and Dias 2018; Seghateh Mojtahedi et al. 2021; Senent et al. 2013; Saada et al. 2013; Chen and Lin 2019; Qin and Chian 2018; Zhao et al. 2017; Maleki and Imani 2022; Hoek et al. 2002). For example, Hoek et al. (2002) proposed the direct equivalent technique to cut the Hoek–Brown strength envelop, and defined the intercept on shear stress axis and inclination as equivalent cohesion and friction angle. However, it is worth noting that the tangent line obtained by the Direct equivalent technique is lower than the Hoek–Brown envelop, so this method fails to obtain the strict upper-bound solutions (Yang et al. 2004; Li et al. 2022). To deal with this drawback, Yang et al. (2004) proposed a tangent method to simplify the nonlinear criterion into a linear one (see Fig. 1a). Because the tangential line in the tangent method exceeds the original non-linear Hoek–Brown envelop, the tangent method can provide an upper-bound estimation for the stability issues (Seghateh Mojtahedi et al. 2021; Chen and Lin 2019; Qin and Chian 2018). Referring to Yang et al. (2004), the tangential line of the nonlinear Hoek–Brown envelop can be expressed as,

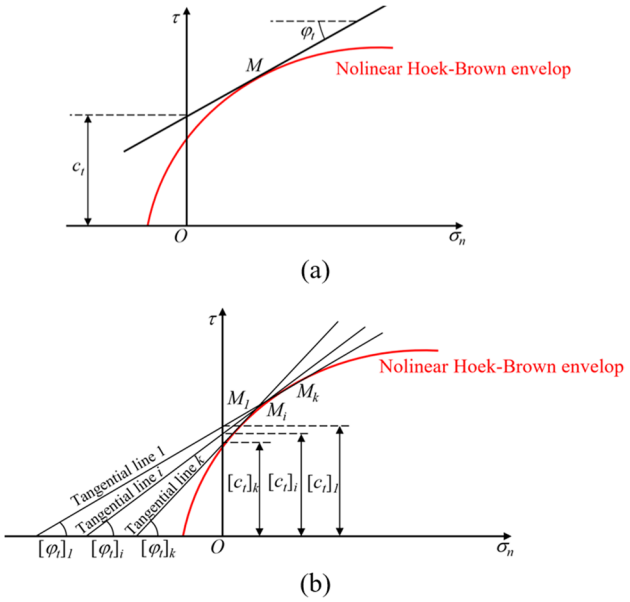

Fig. 1 Tangent method for rock masses **a** traditional tangent method; **b** multi-tangent method

$$\tau = c_t + \sigma_n \tan\varphi_t \tag{5}$$

where c_t is the equivalent cohesion; φ_t is the equivalent friction angle. c_t can be written as a function of φ_t as follows,

$$\begin{aligned} c_t = f\left(m_i, GSI, \sigma_{ci}, D_i, \varphi_t\right) &= \frac{\sigma_{ci}\cdot\cos\varphi_t}{2}\left[\frac{m_b\cdot a\left(1-\sin\varphi_t\right)}{2\cdot\sin\varphi_t}\right]^{\frac{a}{1-a}} \\ &- \frac{\sigma_{ci}\cdot\tan\varphi_t}{m_b}\left(1+\frac{\sin\varphi_t}{a}\right)\left[\frac{m_b\cdot a\left(1-\sin\varphi_t\right)}{2\cdot\sin\varphi_t}\right]^{\frac{1}{1-a}} \\ &+ \frac{s}{m_i}\cdot\sigma_{ci}\cdot\tan\varphi_t \end{aligned} \tag{6}$$

Note that, in Eq. (6), φ_t is an additional optimization parameter compared with the Mohr–Coulomb failure criterion. Since Yang et al. (2004), the tangent method has been extensively adopted in the stability analysis of various engineering structures in rock masses (Seghateh Mojtahedi et al. 2021; Chen and Lin 2019; Qin and Chian 2018; Zhao et al. 2017; Maleki and Imani 2022). However, the traditional tangent method introduced above is merely employed single tangent line to substitute the nonlinear Hoek–Brown failure criterion, which will definitely reduce the accuracy of the results (Mao et al. 2012). To solve this shortcoming, a multi-tangent method is introduced and adopted to determine the equivalent Mohr–Coulomb parameters of rock masses in this study (see Fig. 1b). As shown in Fig. 1b, the nonlinear Hoek–Brown failure criterion is linearly cut by several tangential lines, which ensures the varying equivalent cohesions and friction angles at the velocity discontinuity

surfaces of the failure model. This assists in searching for the global optimum during the optimization operation (Mao et al. 2012). Combining Eq. (6), the expression of equivalent cohesions using the multi-tangent method can be obtained by,

$$\begin{Bmatrix} [c_t]_1 \\ \cdots \\ [c_t]_i \\ \cdots \\ [c_t]_k \end{Bmatrix} = \begin{Bmatrix} f(\sigma_{ci}, m_i, GSI, D_i, [\varphi_t]_1) \\ \cdots \\ f(\sigma_{ci}, m_i, GSI, D_i, [\varphi_t]_i) \\ \cdots \\ f(\sigma_{ci}, m_i, GSI, D_i, [\varphi_t]_k) \end{Bmatrix} \tag{7}$$

where $[\varphi_t]_1$, $[\varphi_t]_i$, and $[\varphi_t]_k$ are the equivalent friction angles for tangential line 1, tangential line i, and tangential line k; k denotes the number of tangential lines adopted to cut the nonlinear Hoek–Brown envelop (see Fig. 1b). For simplicity, each rock layer is uniformly divided into k layers in vertical direction, and the equivalent Mohr–Coulomb parameters for each rock layer are calculated based on the corresponding tangential line. That is, for ith layer, the corresponding equivalent friction angle and cohesion are $[\varphi_t]_i$ and $[c_t]_i$ (see Fig. 1b). Therefore, compared with the traditional tangent method, more optimization parameters $[\varphi_t]_i$ ($i=2,3\ldots,k$) are required in the optimization operation, thus determining of the global optimum of the objective function, i.e., the limit support pressure in this study. Obviously, a better optimal value is associated to a larger k. However, a larger k means a longer computation time. Therefore, a suitable value of k should be first determined to ensure the computation efficiency without affecting the accuracy of results.

In order to study the influence of number of tangential line k on the accuracy and efficiency of the optimization issue, a series of limit support pressures and corresponding calculation times with different k are obtained by using the analytical method developed in this study (see Fig. 2). Figure 2a shows the problem statement, and the obtained results are provided in Fig. 2b. It can be seen in Fig. 2a that the rock masses in the study zone is uniformly divided into k layers. Considering the magnitude of the failure model (Zou et al. 2019a, b; Di et al. 2023a, b, c), the width and height of the study zone are assumed to be $1.5D$ and $2D$ (see Fig. 2a). The parameters adopted in Fig. 2b are as follows: $D=10$m, $GSI=10$, $m_i=5$, $\sigma_{ci}=1$MPa, $D_i=0$, and $\gamma=25$kPa. The computer used in the calculation is Intel(R) Core (TM) i5-10400F CPU 2.90GHz. From Fig. 2b, it can be seen that, as k increases, the increasing ratio of limit support pressure σ_T gradually decreases. This illustrates that the larger upper-bound solution can be obtained with higher k. However, in Fig. 2b, one can also find that the calculation time nearly exponentially increases as k increases. For example, the calculation time is 564s for $k=1$, but 2195s for $k=7$. This indicates that the increasing of k has strong negative impact on the computational efficiency. To synthesize the computational accuracy and efficiency, $k=3$ is adopted to determine the equivalent Mohr–Coulomb parameters of rock masses in this study.

Improved failure models in layered rock masses

In this section, based on the traditional 3D rotational failure model proposed by Mollon et al. (2011), an improved failure model is first developed to make it possible to incorporate the properties of layered rock masses into the stability analysis of the tunnel face. The improved rotational failure model in layered rock masses is presented in Fig. 3. As shown in Fig. 3, two horizontal layered rock masses are assumed in this study (layer 1: σ_{ci1}, m_{i1}, GSI_1, and D_{i1}; layer 2:σ_{ci2}, m_{i2}, GSI_2, and D_{i2}). In Fig. 3b, ηD denotes the distance between the tunnel crest to the intersection between two-layer rock masses. In the traditional rotational failure model, two presumed logarithmic spirals with constant friction angle were adopted to generate the failure boundaries, which results in the difficulty of solving the stability problem of non-homogeneous materials using the traditional rotational failure model. To solve this problem, the discretized failure boundaries are derived using the discretization technique (see Fig. 3b). As shown in Fig. 3b, the discretized boundary BF consists of a series of segments P_iP_{i+1} ($P_1=B$). Therefore, to obtain the discretized boundary BF, the most significant issue is to calculate the point P_{i+1} from point P_i. In this study, the discretization technique (Chen et al. 2023) is adopted to obtain the point $P_{i+1}(y_{i+1},z_{i+1})$ from the given point $P_i(y_i,z_i)$ ($P_1=B$) (see Fig. 3c and Eq. (8)).

$$\begin{cases} y_{i+1} = y_o - \frac{(y_o-y_i)\cdot\cos(\beta_i+[\varphi_t]_i)-(z_o-z_i)\cdot\sin(\beta_i+[\varphi_t]_i)}{\cos(\beta_i+[\varphi_t]_i)\cdot\cos\beta_{i+1}+\sin(\beta_i+[\varphi_t]_i)\cdot\sin\beta_{i+1}} \cdot cos\beta_{i+1} \\ z_{i+1} = z_o + \frac{(y_o-y_i)\cdot\cos(\beta_i+[\varphi_t]_i)-(z_o-z_i)\cdot\sin(\beta_i+[\varphi_t]_i)}{\cos(\beta_i+[\varphi_t]_i)\cdot\cos\beta_{i+1}+\sin(\beta_i+[\varphi_t]_i)\cdot\sin\beta_{i+1}} \cdot sin\beta_{i+1} \end{cases} \tag{8}$$

where $[\varphi_t]_i$ is the equivalent friction angle at point P_i; y_o and z_o are the coordinates of the rotation center O, and can be written as,

$$\begin{cases} y_o = D\cdot\left(\frac{r_E}{D}\cdot\cos\beta_E - \frac{1}{2}\right) \\ z_o = -D\cdot\left(\frac{r_E}{D}\cdot\sin\beta_E\right) \end{cases} \tag{9}$$

where r_E/D and β_E are two optimization parameters in the determination of the upper-bound solution.

Similar to the calculation of the discretized boundary BF, the point $Q_{j+1}(y_{j+1},z_{j+1})$ can be generated using the discretization technique with the given point $Q_j(y_j,z_j)$ ($Q_1=A$) as follows (see Fig. 3d),

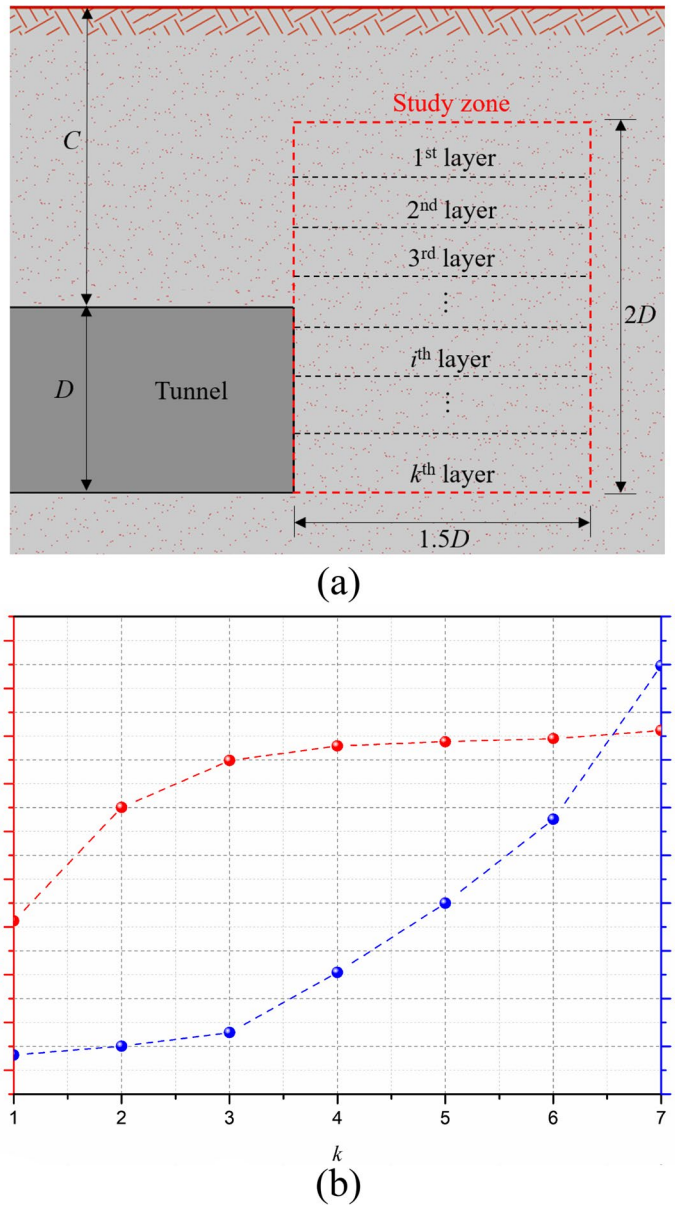

Fig. 2 Effect of k on the accuracy and efficiency of the optimization issue **a** problem statement; **b** limit support pressure and computation time with changing k

$$\begin{cases} y_{j+1} = y_o - \dfrac{(y_o - y_j)\cdot\cos(\varphi_j - \beta_j) + (z_o - z_j)\cdot\sin\left([\varphi_t]_j - \beta_j\right)}{\cos\left([\varphi_t]_j - \beta_j\right)\cdot\cos\beta_{j+1} - \sin\left([\varphi_t]_j - \beta_j\right)\cdot\sin\beta_{j+1}} \cdot cos\beta_{j+1} \\ z_{j+1} = z_o + \dfrac{(y_o - y_j)\cdot\cos\left([\varphi_t]_j - \beta_j\right) + (z_o - z_j)\cdot\sin\left([\varphi_t]_j - \beta_j\right)}{\cos\left([\varphi_t]_j - \beta_j\right)\cdot\cos\beta_{j+1} - \sin\left([\varphi_t]_j - \beta_j\right)\cdot\sin\beta_{j+1}} \cdot sin\beta_{j+1} \end{cases} \tag{10}$$

Then, the tunnel face is discretized around the tunnel center E using the discretization technique (see Fig. 3a). Finally, based on the discretized points at the tunnel face and the boundaries AF and BF, the 3D failure surface for the improved rotational failure model can be obtained using the "point by point" technique (Mollon et al. 2011). Note that, in the generation of 3D failure surface, the constant friction angle is substituted by the spatial varying equivalent friction angles. Note that, the improved rotational failure model presented in Fig. 3 is the whole failure model in layered rock masses. The whole failure model represents that the whole failure happens at the tunnel face (see Fig. 3). Some recently published literatures showed that the upper partial failure within the tunnel face is more likely to happen when there are two-layer materials in the crossed layer of the tunnel face with weak properties in layer 1 and strong properties in layer 2 (Cheng et al. 2019; Senent and Jimenez 2015; Dias et al. 2008; Li et al. 2009). But these published studies are limit to the soil materials, and no attempts have been conducted in layered rock masses. Based on existing numerical results (Dias et al. 2008; Li et al. 2009), a further improved failure model is proposed with considering the possibility of the upper partial failure at the tunnel face for layered rock

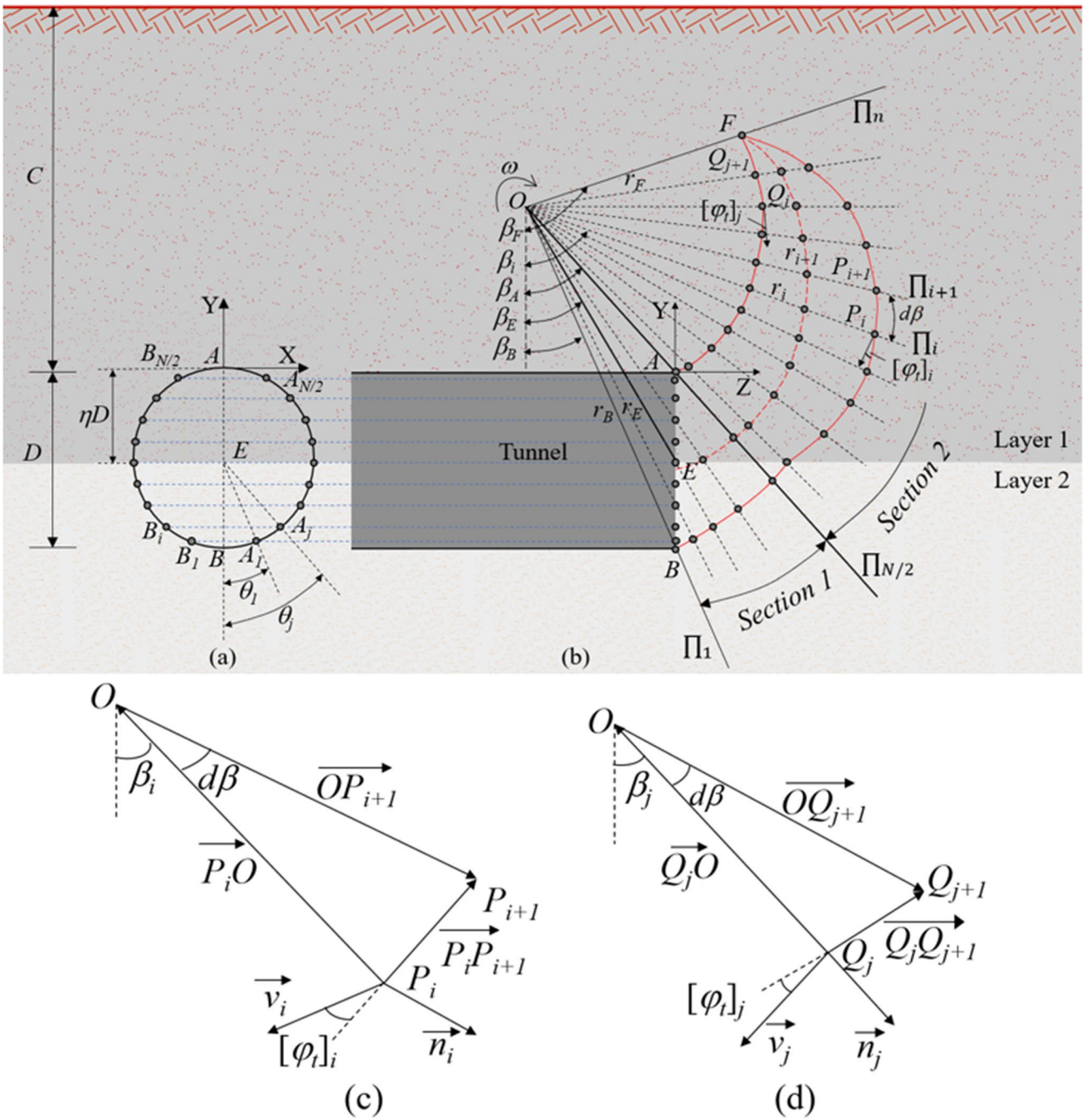

Fig. 3 Improved rotational failure model in layered rock masses **a** discretization of the tunnel face; **b** discretization of the failure boundaries; **c** generation of the discretized boundary *BF*; **d** generation of the discretized boundary *AF*

masses (see Fig. 4). As shown in Fig. 4, the "transition" circular failure zone proposed by Cheng et al. (2019) is adopted to represent the upper partial failure within the tunnel face in layered rock masses. In Fig. 4, the circle E_t and the circle E'_t are internally tangent to the tunnel face, and are symmetric about the central axis *AB* of the tunnel face. According to the geometric conditions, the center of the circle $E_t(x_t,y_t)$ can be calculated by,

$$\begin{cases} x_t = \sqrt{\left(\frac{D}{2} - r_t\right)^2 - \left(\eta \cdot D - \frac{D}{2} - r_t\right)^2} \\ y_t = r_t - \eta \cdot D \end{cases} \tag{11}$$

where ηD is the distance between the tunnel crest to the intersection between two-layer rock masses; r_t is the radius of the circle E_t (see Fig. 4). Note that, in Eq. (11), the entire

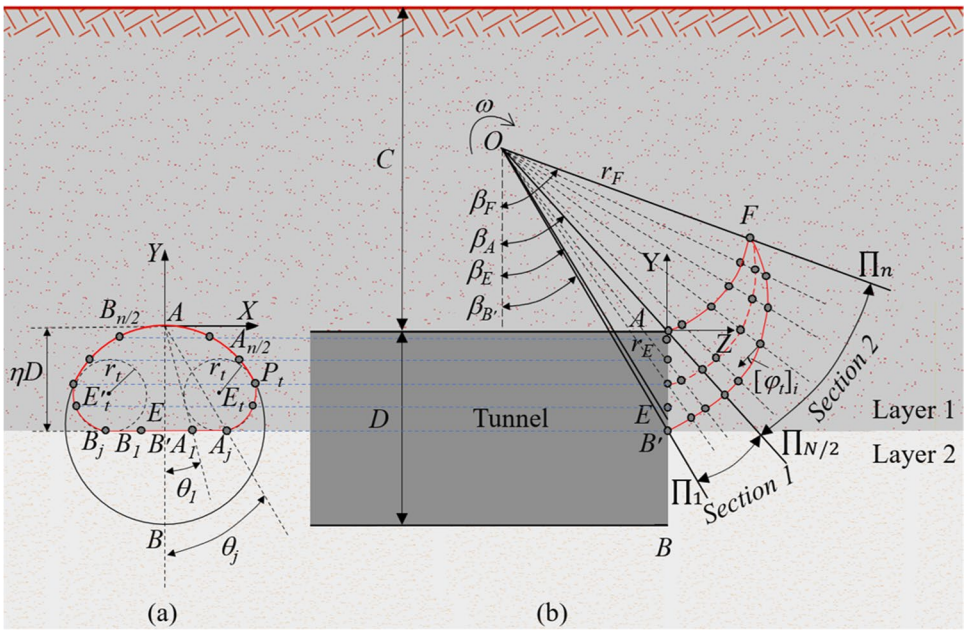

Fig. 4 Improved failure model considering the upper partial failure **a** discretization of the tunnel face; **b** discretization of the failure boundaries

upper partial failure will happen when $r_t = 0$. As shown in Fig. 4, the intersection $P_t(x_{Pt},y_{Pt})$ between the circle E_t and the tunnel face can be described as,

$$\begin{cases} x_{Pt} = \frac{x_t \cdot D}{D-2 \cdot r_t} \\ y_{Pt} = \frac{y_t \cdot D + D \cdot r_t}{D-2 \cdot r_t} \end{cases} \tag{12}$$

Different from the improved rotational failure model presented in Fig. 3, the discretization of upper partial failure model at the tunnel face is around the tunnel crest (the point A), and can be divided into following three parts:

Part 1: the coordinates of discretization point $A_j(x_j,y_j)$ for $0 \le \theta_j \le \arctan(x_t/\eta D)$ can be written as,

$$\begin{cases} x_j = \eta \cdot D \cdot tan\theta_j \\ y_j = -\eta \cdot D \end{cases} \tag{13}$$

Part 2: the coordinates of discretization point $A_j(x_j,y_j)$ for $\arctan(x_t/\eta D) < \theta_j \le \arctan(-x_{Pt}/y_{Pt})$ can be written as,

$$\begin{cases} x_j = \frac{1}{\cot^2\theta_j + 1} \cdot \left(x_t + \sqrt{-\cot^2\theta_j \cdot x_t^2 + \cot^2\theta_j \cdot r_t^2 - 2 \cdot x_t \cdot y_t \cdot \cot\theta_j - y_t^2 + r_t^2} - y_t \cdot \cot\theta_j \right) \\ y_j = -\frac{\cot\theta_j}{\cot^2\theta_j + 1} \left(x_t + \sqrt{-\cot^2\theta_j \cdot x_t^2 + \cot^2\theta_j \cdot r_t^2 - 2 \cdot x_t \cdot y_t \cdot \cot\theta_j - y_t^2 + r_t^2} - y_t \cdot \cot\theta_j \right) \end{cases} \tag{14}$$

Part 3: the coordinates of discretization point A_j (x_j,y_j) for $\arctan(-x_{Pt}/y_{Pt}) < \theta_j \le \pi/2$ can be written as,

$$\begin{cases} x_j = \frac{1}{2} \cdot D \cdot sin\left(2 \cdot \theta_j\right) \\ y_j = -\frac{1}{2} \cdot D \cdot \left[\cos\left(2 \cdot \theta_j\right) + 1\right] \end{cases} \tag{15}$$

Once the discretization points of the upper partial failure model at the tunnel face are calculated, the improved rotational failure model with considering the upper partial failure can be obtained using the discretization and "point by point" techniques (Mollon et al. 2011).

Upper-bound solutions in layered rock masses

Referring to Mollon et al. (2011) and Chen et al. (2022), the upper bound limit analysis approach is employed to determine the limit support pressure of the tunnel face by equating the internal energy dissipation rate to the work done by external forces as follows,

$$W_{\sigma_T} = D_c - W_\gamma \tag{16}$$

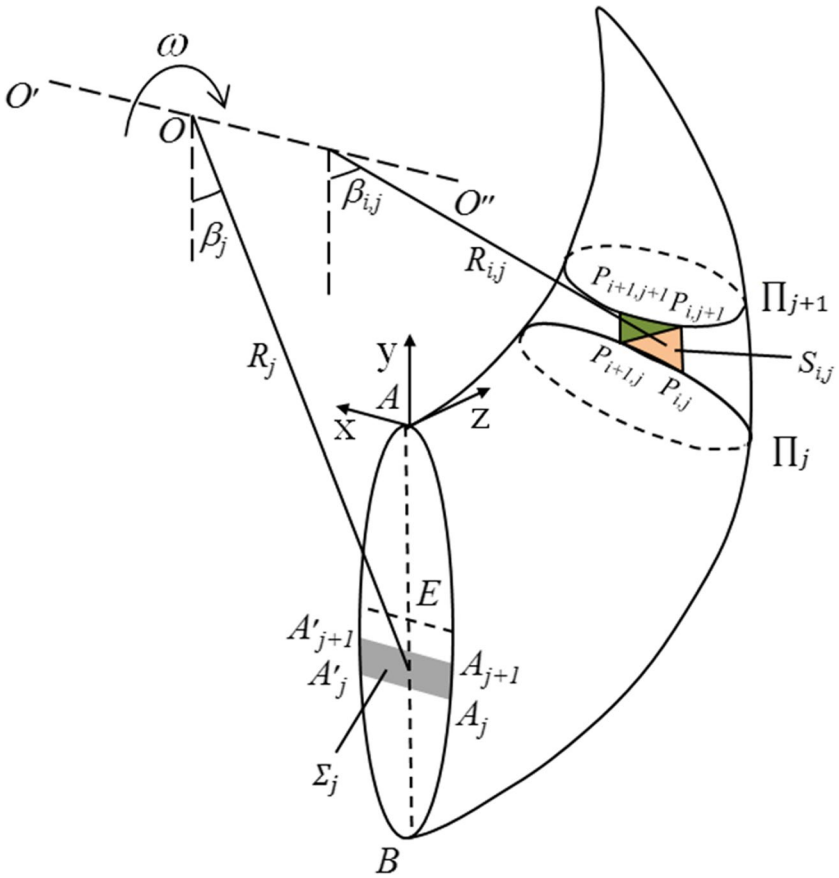

Fig. 5 View of work calculations

where D_c is the internal energy dissipation rate along the 3D failure surface; W_γ is the work due to the gravity of rock masses; W_{σ_T} is the work done by the supporting pressure.

As shown in Fig. 5, the internal energy dissipation rate D_c can be expressed as,

$$D_c = \iint_S c_t \cdot |\vec{v}| \cdot \cos\varphi_t dS = \omega \cdot \sum_{i,j} \left([c_t]_{i,j} \cdot R_{i,j} \cdot S_{i,j} \cdot \cos[\varphi_t]_{i,j} \right) \tag{17}$$

where $S_{i,j}$ is the element surface at the 3D failure surface; $R_{i,j}$ is the rotation radius of the element surface $S_{i,j}$; $[c_t]_{i,j}$ is the equivalent cohesion at the element surface $S_{i,j}$; $[\varphi_t]_{i,j}$ is the equivalent friction angle at the element surface $S_{i,j}$.

The work done by the gravity of rock masses W_γ can be calculated by,

$$W_\gamma = \iiint_V \vec{\gamma} \cdot \vec{v} dV = \omega \cdot \sum_{i,j} \left(\gamma_{i,j} \cdot R_{i,j} \cdot V_{i,j} \cdot \sin\beta_{i,j} \right) \tag{18}$$

where $V_{i,j}$ is the element volume of the failure model; $R_{i,j}$ is the rotation radius of the element volume $V_{i,j}$; $\beta_{i,j}$ is the rotation angle of the element volume $V_{i,j}$; $\gamma_{i,j}$ is the unit rock weight at the element volume $V_{i,j}$.

The work due to the supporting pressure acting on the tunnel face W_{σ_T} can be described as,

$$W_{\sigma_T} = \iint_\Sigma \vec{\sigma}_T \cdot \vec{v} d\sum = \omega \cdot \sigma_T \cdot \sum_j \left(R_j \cdot \sum_j \cdot \cos\beta_j \right) \tag{19}$$

where $\sum_j$ is the element face of the tunnel face; R_j is the rotation radius of the element face $\sum_j$; β_j is the rotation radius of the element face $\sum_j$.

Combining Eqs. (16) to (19), the limit support pressure σ_{T1} for the whole failure model can be determined by maximizing Eq. (20) with respect to optimization parameters r_E/D, β_E, $[\varphi_{t1}]_i$ and $[\varphi_{t2}]_i$ $(i = 1,2,3)$ as follows,

$$\sigma_{T1} = \max_{(r_E/D, \beta_E, [\varphi_{t1}]_i, [\varphi_{t2}]_i)} \left(N_\gamma - N_c \right) \tag{20}$$

with

$$\begin{cases} 0.5 \le \frac{r_E}{D} \le 20 \\ 1^\circ \le \beta_E < 90^\circ \\ 1^\circ \le [\varphi_{t1}]_i \le 45^\circ \\ 1^\circ \le [\varphi_{t2}]_i \le 45^\circ \end{cases} \tag{21}$$

The limit support pressure σ_{T2} for the upper partial failure model can be calculated by maximizing Eq. (22) with respect to optimization parameters r_E/D, β_E, r_t, and $[\varphi_t]_i$ $(i = 1,2,3)$ and as follows,

$$\sigma_{T2} = \max_{(r_E/D,\beta_E,r_t,[\varphi_{t1}]_i)} \left(N_\gamma - N_c\right) \tag{22}$$

with

$$\begin{cases} 0.5 \le \frac{r_E}{D} \le 20 \\ 1^\circ \le \beta_E < 90^\circ \\ 0 \le r_t \le \frac{\eta \cdot D}{2} \\ 1^\circ \le \left[\varphi_{t1}\right]_i \le 45^\circ \end{cases} \tag{23}$$

To calculate the limit support pressure, the widely adopted optimization algorithm is the unconstrained optimization tool (fminsearch) in MATLAB (Pan and Dias 2016a; Zou et al. 2019b). However, this optimization algorithm is intractable to search the global optimal value when the number of optimization parameters is more than four. To solve this issue, the genetic algorithm was introduced and adopted by Xu and Du (2023) to accurately assess the slope stability under multi-optimization parameters. Based on it, the genetic algorithm is employed to determine the limit support pressure of the tunnel face under multi-optimization parameters in this study. Because the limit support pressure for the tunnel face is the upper-bound solution for layered rock masses, the final limit support pressure is the maximum of Eq. (20) and Eq. (22) as follows,

$$\sigma_T = \max\left(\sigma_{T1}, \sigma_{T2}\right) \tag{24}$$

Note that, in Eq. (20) and Eq. (22), N_γ and N_c respectively denotes the influence of the rock weight and the equivalent cohesion on the limit support pressure, and can be expressed as,

$$N_\gamma = \frac{\sum\limits_{i,j} \left(\gamma_{i,j} \cdot R_{i,j} \cdot V_{i,j} \cdot \sin\beta_{i,j}\right)}{\sum\limits_{j} \left(R_j \cdot \sum\limits_{j} \cdot \cos\beta_j\right)} \tag{25}$$

$$N_c = \frac{\sum\limits_{i,j} \left(\left[c_t\right]_{i,j} \cdot R_{i,j} \cdot S_{i,j} \cdot \cos\left[\varphi_t\right]_{i,j}\right)}{\sum\limits_{j} \left(R_j \cdot \sum\limits_{j} \cdot \cos\beta_j\right)} \tag{26}$$

Figure 6 provides the limit support pressures and corresponding 3D failure surfaces for the cases of two-layer rock masses with $D = 10$m, $\eta = 0.5$, and $\gamma_1 = \gamma_2 = 25$kN/m^3. The parameters adopted in Fig. 6a are as follows: layer 1 ($m_{i1} = 5$, $GSI_1 = 10$, $\sigma_{ci1} = 1$MPa, and $D_{i1} = 0$); layer 2 ($m_{i2} = 5$, $GSI_2 = 20$, $\sigma_{ci2} = 2$MPa, and $D_{i2} = 0$). The parameters adopted in Fig. 6b are as follows: layer 1 ($m_{i1} = 5$, $GSI_1 = 10$, $\sigma_{ci1} = 1$MPa, and $D_{i1} = 0$); layer 2 ($m_{i2} = 10$, $GSI_2 = 20$, $\sigma_{ci2} = 3$MPa, and $D_{i2} = 0$). From Fig. 6a, it can be seen that the whole failure at the tunnel face happens, and there exists an obvious transition in the 3D failure surface at the intersection between two-layer rock masses, which is consistent to the results observed by Man et al. (2022a, 2022b) using the 2D log-spiral failure model. From Fig. 6b, it can be found that the upper partial failure at the tunnel face occurs for this selected case. Combining Fig. 6a and b, one can conclude that the possibility of upper partial failure will increase as properties of lower layer increase.

Validation of the proposed method

Validation in soil masses

Validation with published solutions

Firstly, a comparison between the limit support pressures obtained from the proposed method and published solutions from Senent and Jimenez (2015) are presented in Table 1. The parameters adopted in Table 1 are as follows: $D = 10$m, $\eta = 0.5$, $[\varphi_t]_1 = 30^\circ$, $[\varphi_t]_2 = 30^\circ$, $[c_t]_1 = 0$–35kPa, $[c_t]_2 = 0$kPa, and $\gamma_1 = \gamma_2 = 20$kN/m^3.

From Table 1, it can be seen that, for these selected cases, the whole failure will occur when $[c_t]_1 \le 15$kPa, and the partial failure will happen when $[c_t]_1 > 15$kPa. Also, from Table 1, one can find that the analytical solutions obtained by Senent and Jimenez (2015) are slightly larger than the numerical results with the average difference up to 4.5%, and the limit support pressures calculated from the proposed method are closer to the numerical results with average difference less than 2.2%. This observation illustrates that the proposed method is an effective approach to investigate the tunnel face stability in layered materials.

Validation based on practical tunnel engineering

Then, the proposed method is validated based on practical tunnel engineering. Figure 7 shows the geological section from Qili Station to Minxiluxi Station in Nanchang Metro Line 4, which is located in Nanchang, China. The total length of this section is 2017m. The tunnel was excavated by using a circular shield machine with an excavation diameter of 6m. The study zone in this section is shown in Fig. 8. The soil parameters in the study zone are summarized in Table 2.

Based on the proposed method, the limit support pressure and corresponding failure surface can be obtained, as shown in Fig. 9. To validate the proposed method, a numerical analysis based on the finite element limit analysis (Zhang et al. 2019) is conducted. Figure 10 presents the comparison between the results from the proposed method and numerical analysis. From Fig. 10, it can be seen that the limit support pressure calculated from the proposed method is slightly

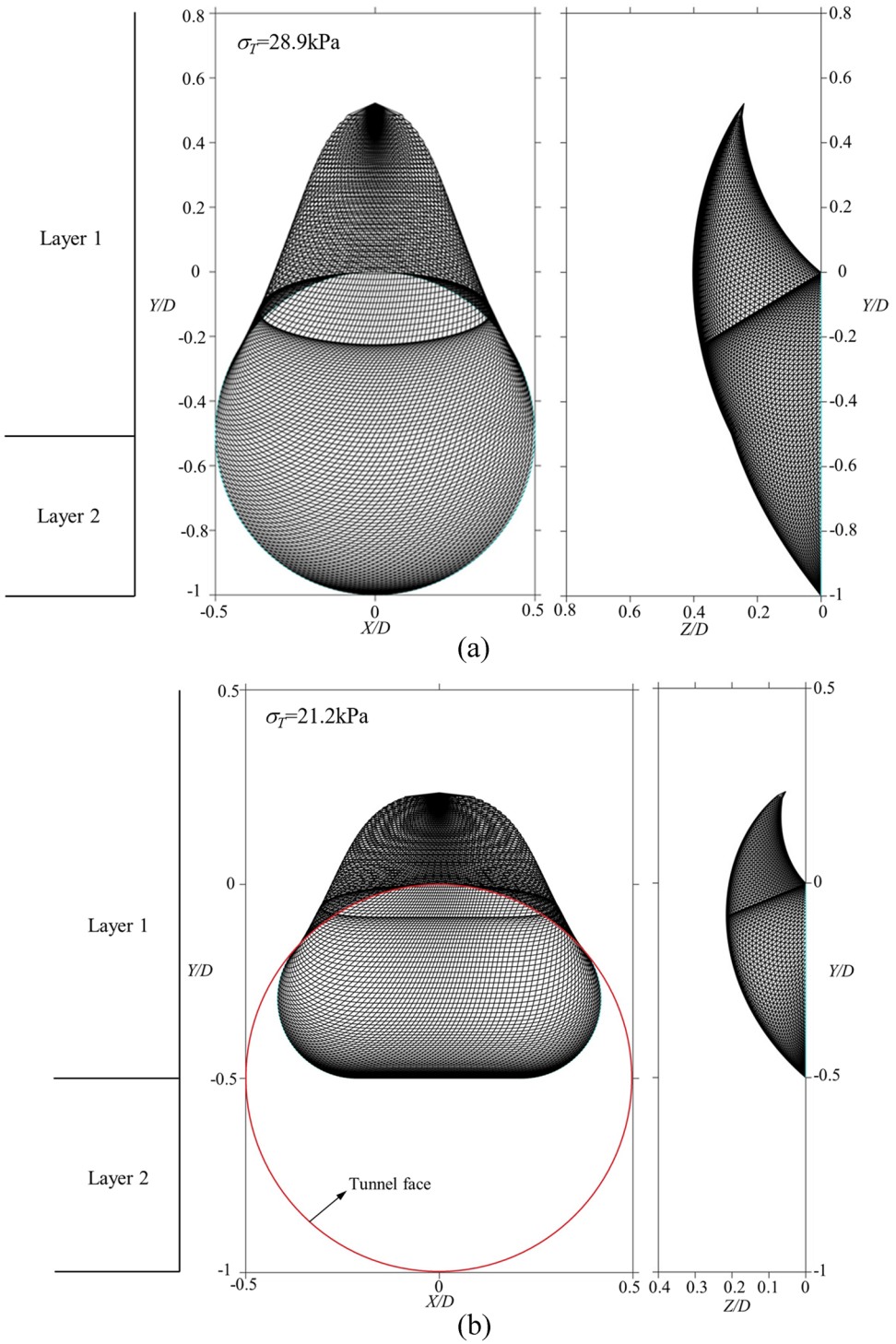

Fig. 6 Failure surfaces based on the proposed method **a** 3D whole failure surface; **b** 3D upper partial failure surface

lower than the numerical result with the difference less than 6%, and both analytical solution and numerical result are smaller than the practical engineering design value (15kPa) considering a certain security reserve. Also, one can find that the failure surface from the proposed method is slightly smaller than the numerical one in Fig. 10. These observations further illustrate the effectiveness of the proposed method.

Validation in rock masses

To validate the proposed method in rock masses, a comparison between the limit support pressures calculated by the proposed method with existing analytical solutions (Senent et al. 2013) and numerical results is first conducted for homogeneous rock masses. Then, the comparisons

Table 1 Validation with published solutions in layered materials (unit: kPa)

$[c_t]_1$	Analytical solutions (Senent and Jimenez 2015)		Numerical solutions (Senent and Jimenez 2015)	This study
	$\sigma_{T,global}$	$\sigma_{T,partial}$		
0	29.2	16.5	27.3	28.2
5	25.3	16.5	23.3	24.3
10	21.4	16.5	19.9	21
15	17.7	16.5	17.3	17.3
20	14.1	16.5	16.2	15.9
25	10.6	16.5	16	15.9
30	7.1	16.5	16	15.9
35	3.9	16.5	16.1	15.9

between the limit support pressures obtained from the proposed method and numerical results are provided for layered rock masses. Figure 11 shows the established numerical model based on the FLAC3D. As shown in Fig. 11, the numerical model is large enough with length = 8D, width = 5D, and height = 8D. The bottom of the numerical model is full fixed; the vertical faces of the numerical model are fixed in the normal directions; the top of the numerical model is free to displace. Referring to Pan and Dias (2018), the shell of the excavation tunnel is denoted by a linear structural element with Poisson's ratio = 0.2, Young's modulus = 20GPa, and thickness = 22mm. In the numerical model, the rock masses are assumed to obey the Hoek–Brown failure criterion. From Senent et al. (2013), it can be concluded that the divergences of results calculated based on the associated flow rule and the non-associated flow rule are limited, and adopting the associated flow rule to assess the tunnel face stability is acceptable. Therefore, for simplicity, the associated flow rule is assumed in the analytical and numerical analysis in this study. To validate

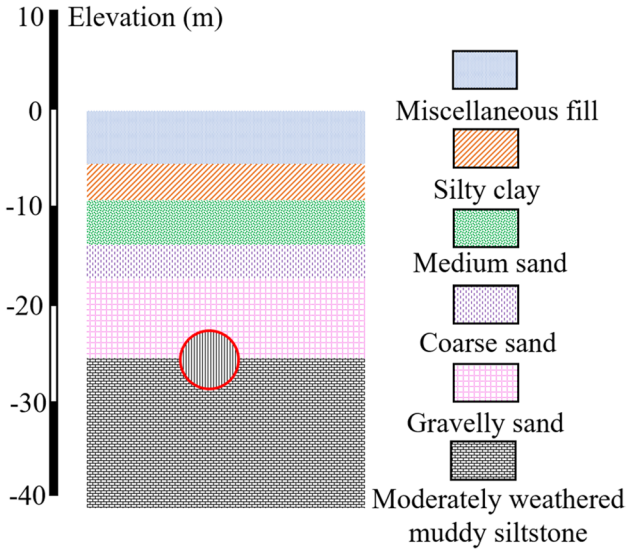

Fig. 8 The study zone in this section

Table 2 Soil parameters in the study zone

Soil	γ (kN/m^3)	$[c_t]$ (kPa)	$[\varphi_t]$ (°)
Miscellaneous fill	18	10	10
Silty clay	18	29.3	17.4
Medium sand	19	0	28
Coarse sand	19.8	0	31
Gravelly sand	20	0	30
Moderately weathered muddy siltstone	25	350	32

the proposed method in layered rock masses, two-layer rock masses are adopted with layer 1 (m_{i1}, GSI_1, σ_{ci1}, D_{i1}, E_{m1}, and v_{m1}) and layer 2 (m_{i2}, GSI_2, σ_{ci2}, D_{i2}, E_{m2} and v_{m2}). E_{m1} and E_{m2} respectively represent the Young's modulus of the rock

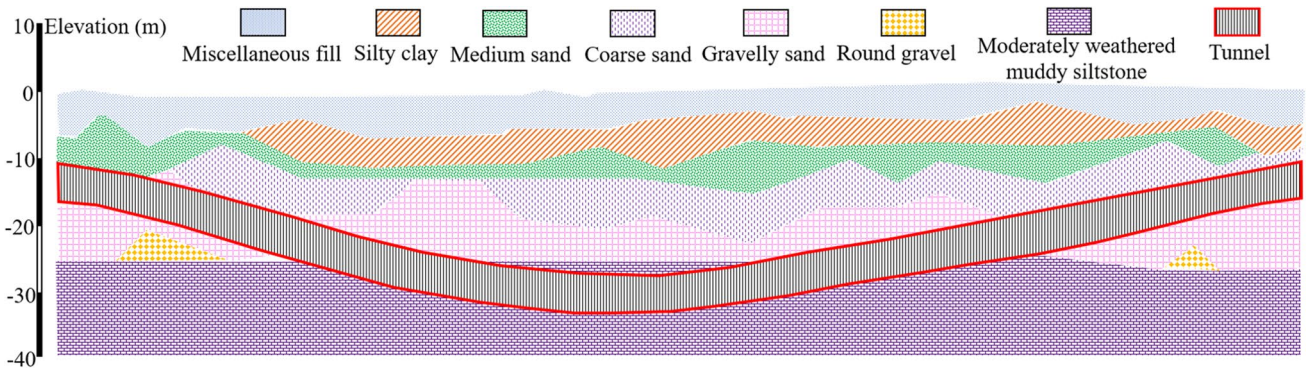

Fig. 7 Geological section from Qili Station to Minxiluxi Station in Nanchang Metro Line 4

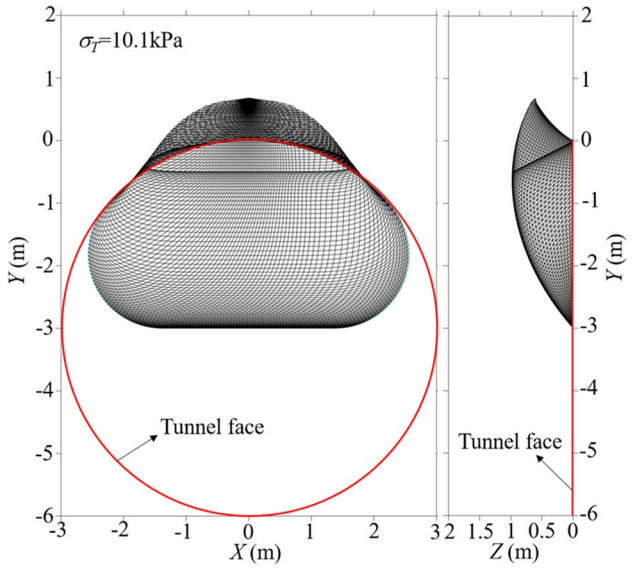

Fig. 9 Limit support pressure and corresponding failure surface for the study zone

mass in layer 1 and layer 2, and can be calculated by (Hoek and Diederichs 2006),

$$\begin{cases} E_{m1} = 10^5 \cdot \left\{ \frac{1-0.5 \cdot D_{i1}}{1+\exp[(75+25 \cdot D_{i1}-GSI_1)/11]} \right\} \\ E_{m2} = 10^5 \cdot \left\{ \frac{1-0.5 \cdot D_{i2}}{1+\exp[(75+25 \cdot D_{i2}-GSI_2)/11]} \right\} \end{cases} \quad (27)$$

v_{m1} and v_{m2} respectively represent the passion ratio of the rock mass in layer 1 and layer 2, and can be expressed as (Vásárhelyi 2009),

$$\begin{cases} v_{m1} = -0.002 \cdot GSI_1 - 0.003 \cdot m_{i1} + 0.457 \\ v_{m2} = -0.002 \cdot GSI_2 - 0.003 \cdot m_{i2} + 0.457 \end{cases} \quad (28)$$

In order to determine the limit support pressure using the numerical model, the supporting forces at the tunnel face are gradually reduced from an appropriately large value (500kPa in this study), and the corresponding horizontal displacements of control point (maximum displacement point) at the tunnel face are recorded for each iteration of the calculation. Figure 12 shows the relationship between the supporting forces with the corresponding horizontal displacements of the control point. The limit support pressure corresponds to the sharp change point of the displacement for the control point, where the collapse failure of the tunnel face first happens (Zou et al. 2019a). In Fig. 12, it can be seen that the limit support pressures for these two selected cases are respectively equal to 56.3kPa and 22.0kPa.

Validation in homogeneous rock masses

Figure 13 presents the comparisons between the limit support pressures calculated by the proposed method with those from Senent et al. (2013) and numerical results in homogeneous rock masses for D=10m, m_i=5, σ_{ci}=1MPa, D_i=0, and γ=25kN/m^3. In Senent et al. (2013), a single tangent

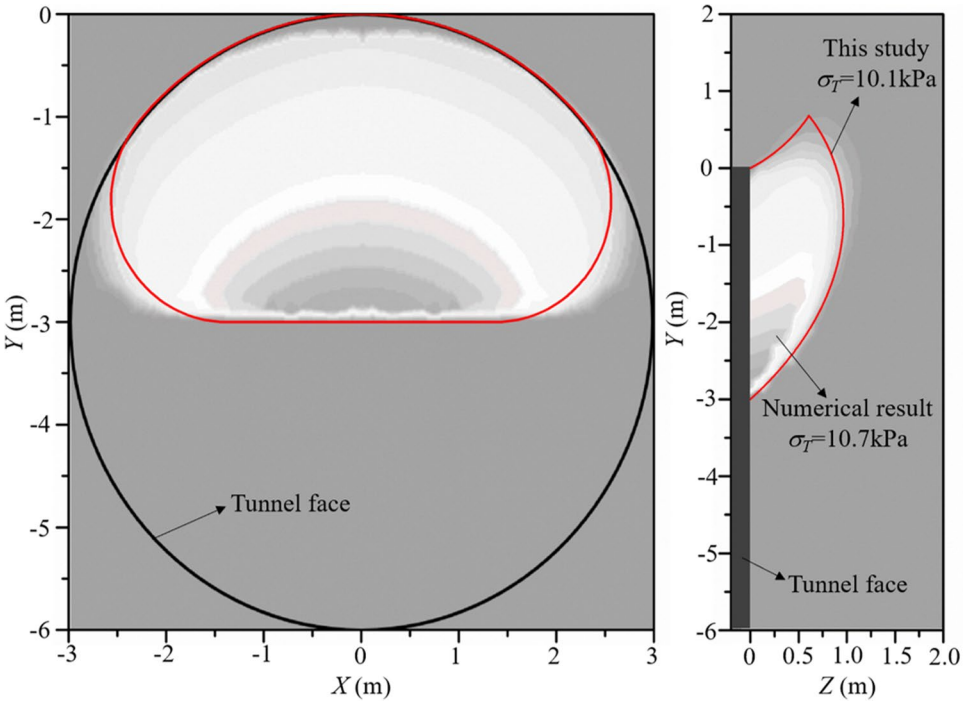

Fig. 10 Validation of the proposed method based on numerical analysis

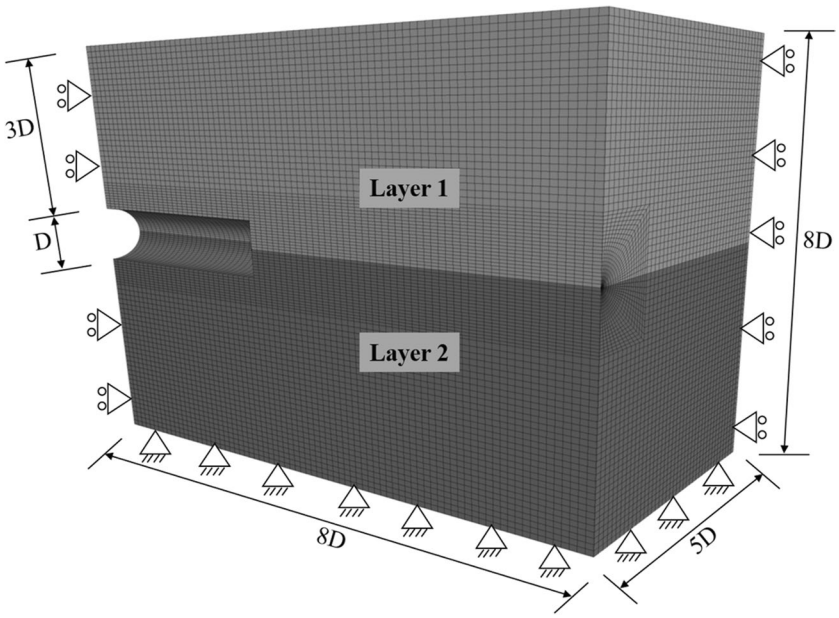

Fig. 11 Numerical model

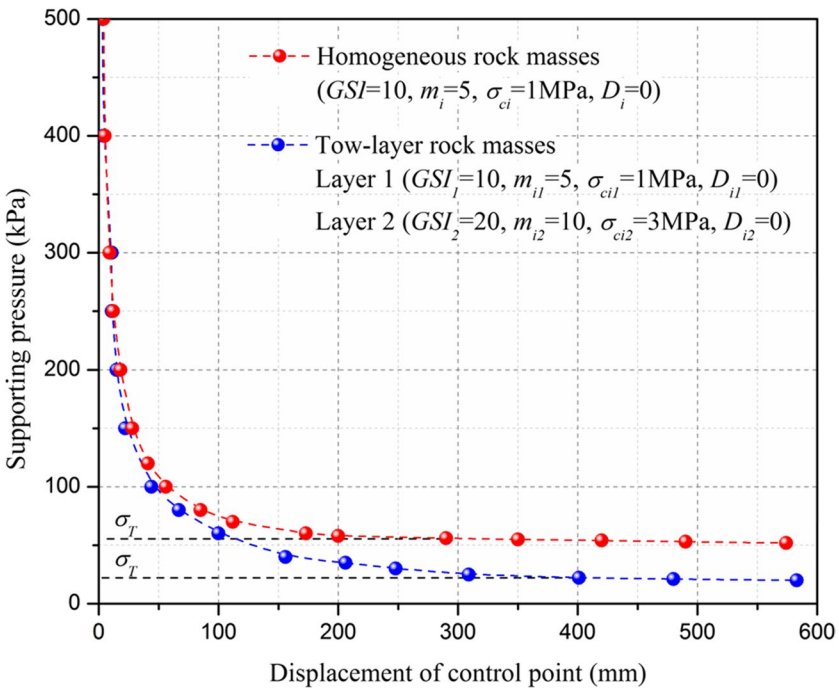

Fig. 12 Calculation of limit support pressures using the numerical model

line was employed to cut the non-linear Hoek–Brown envelop to calculate equivalent Mohr–Coulomb parameters of rock masses. It can be seen in Fig. 13 that the numerical results are slightly higher than those from the proposed method and Senent et al. (2013). From Fig. 13, one can also find that the limit support pressures obtained from the proposed method are closer to the numerical results when compared with those from Senent et al. (2013). The biggest difference is less than 5.8% between results from the proposed method and Senent et al. (2013), and less than 2.2% between the proposed method and numerical results. This indicates that the proposed method using multi-tangent method can provide more accurate estimations for the tunnel face stability. Moreover, because of numerous iterative calculations, it takes more than 300 min to obtain one numerical result. But it only takes approximately 10 min to calculate the analytical solution using the proposed method. These observations indicate that the proposed method is an effective approach to analyze the tunnel face stability in homogeneous rock masses.

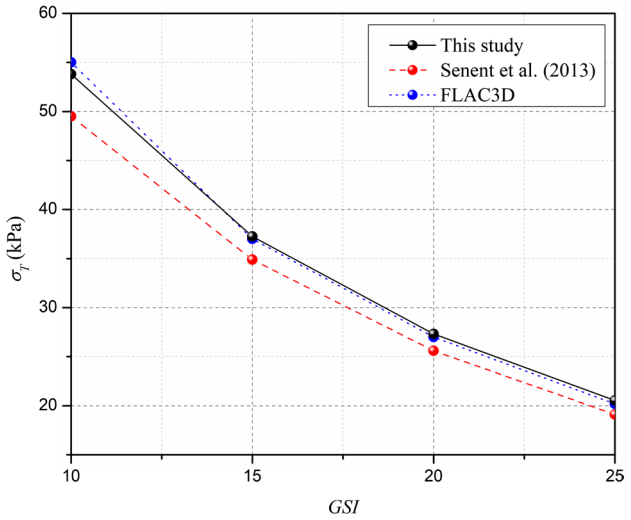

Fig. 13 Validation of the proposed method in homogeneous rock masses

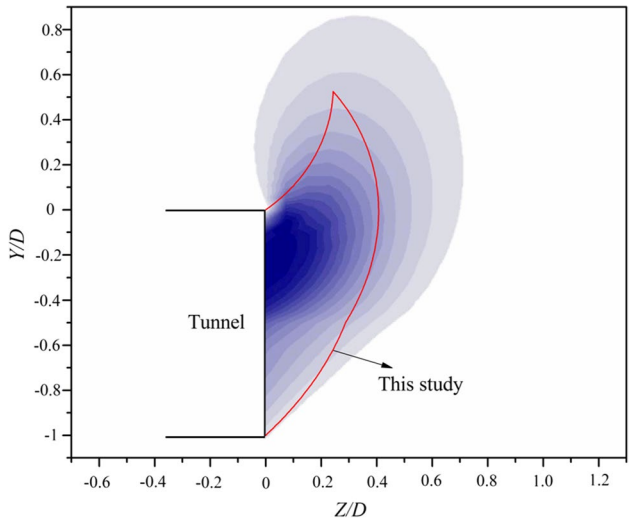

Fig. 14 Comparisons between the failure surfaces from the proposed method and the numerical model for case 3

Validation in layered rock masses

Table 3 shows the comparisons between the limit support pressures calculated by the proposed method with numerical results for five cases with $D=10$m and $\gamma_1=\gamma_2=25$kN/m^3 in layered rock masses. In these five cases, two rock layers are assumed with $\eta=0.5$, and the material properties of rock masses in the upper layer are as follows: $GSI_1=10$, $m_{i1}=5$, $\sigma_{ci1}=1$MPa, and $D_{i1}=0$. From Table 3, it can be seen that the limit support pressures obtained in this study is slightly lower than the numerical results with the biggest difference less than 3.6%. Moreover, one can also find that the limit support pressure varies with the changing of material properties in the lower layer when the whole failure happens, but remains constant when the upper partial failure occurs. To better validate the proposed method, the comparisons between the failure surfaces obtained by the proposed method and the numerical model are presented for case 3 and case 5, as shown in Figs. 14 and 15. From Figs. 14 and 15, one can see that failure surface obtained in the numerical model is slightly wider than the one from the proposed method, but the failure surface obtained in this study covers main deformation zone of the rock masses observed in the numerical model. From Fig. 14, it can be found that the whole failure at the tunnel face occurs for case 3, and both failure surfaces from the proposed method and the numerical model for case 3 have obvious transitions at the intersection between two-layer rock masses. From Fig. 15, it can be seen that, for case 5, both of the failure surfaces calculated by the proposed method and the numerical model are upper partial failures at the tunnel face, which indicates that the upper partial failure happens for case 5. These observations illustrate that the proposed method is an effective approach to analyze the tunnel face stability in layered rock masses.

Results and discussions

In this section, the limit support pressures obtained from the proposed method are first presented with changing rock properties in lower layer for $D=10$m, $\eta=0.5$, $GSI_1=10$, $m_{i1}=5$, $\sigma_{ci1}=1$MPa, and $\gamma_1=\gamma_2=25$kN/m^3 (see Fig. 16). Because shield tunnel excavation has nearly no disturbance to the intact rock, $D_{i1}=D_{i2}=0$ is adopted in the parametric analysis (Seghateh Mojtahedi et al. 2021). To better study the effect of rock properties on the tunnel face stability, the longitudinal sections of the 3D failure surfaces with changing rock properties are plotted in Fig. 17.

Table 3 Validation of the proposed method in layered rock masses

Case	GSI_2	m_{i2}	σ_{ci2} (MPa)	FLAC3D (kPa)	This study (kPa)	Failure type
1	20	5	1.5	34.5	33.6896	Whole failure
2	10	10	2	31.3	30.6176	Whole failure
3	20	5	2	30.5	29.5936	Whole failure
4	20	10	3	22.0	21.216	Upper partial failure
5	30	10	5	22.0	21.216	Upper partial failure

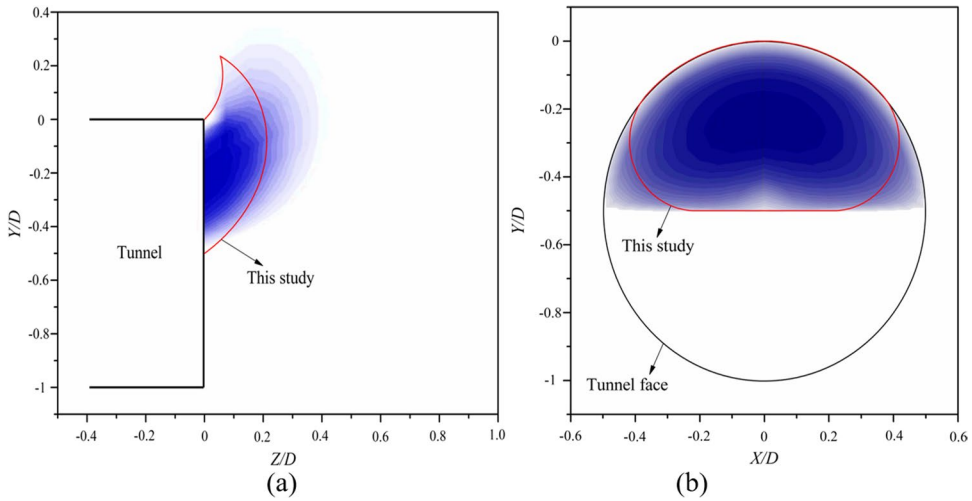

Fig. 15 Comparisons between the failure surfaces from the proposed method and the numerical model for case 5 **a** at the longitudinal section of the failure surface; **b** at the tunnel face

From Fig. 16, it can be seen that the normalized limit support pressure $\sigma_T/\gamma D$ first decreases and then remains constant with the rock properties (GSI_2,m_{i2},σ_{ci2}) increase. This observation can be attributed to the fact that the whole failure within the tunnel face will happen for weak rock properties in the lower layer, and the upper partial failure will occur when the rock property (GSI_2, m_{i2}, or σ_{ci2}) reaches a certain value in the lower layer (see Fig. 17). For example, for $\sigma_{ci2}=1$MPa and $m_{i2}=5$, when $GSI_2<45$, the whole failure of the tunnel face will happen, and the upper partial failure of the tunnel face will happen when $GSI_2\geq 45$ (see Fig. 17a); for $\sigma_{ci2}=1$MPa and $GSI_2=10$, when $m_{i2}<35$, the whole failure will happen, and the upper partial failure of the tunnel face will happen when $m_{i2}\geq 35$ (see Fig. 17b); for $m_{i2}=5$ and $GSI_2=10$, when $\sigma_{ci2}<12$MPa, the whole failure will happen, and the upper partial failure of the tunnel face will happen when $\sigma_{ci2}\geq 12$MPa (see Fig. 17c). From Fig. 17, one can also find that the magnitude of the failure surface slightly reduces with the rock properties increase when the whole failure happens. This observation can be used to illustrate the decrease of the limit support pressure with the increasing of rock properties before the occurrence of the upper partial failure at the tunnel face. When the upper partial failure happens, the limit support pressure and the failure surface are only related to the rock properties in the upper layer, and the changing of rock properties in the lower layer has no influence on the tunnel face stability (see Fig. 16). Combining Fig. 16 and Fig. 17, one can also conclude that, for whole failure, a larger limit support pressure is associated to a larger failure surface.

Then the effect of η on the tunnel face stability with different m_{i2} is presented in Fig. 18. The adopted parameters are as follows: $D=10$m, $GSI_1=10$, $m_{i1}=5$, $\sigma_{ci1}=1$MPa, $GSI_2=10$, $\sigma_{ci2}=2$MPa, and $\gamma_1=\gamma_2=25$kN/m^3. It can be seen in Fig. 18a that, for $\eta=0.00$ and 0.25, $\sigma_T/\gamma D$ continually decreases as m_{i2} increases; for $\eta=0.50$ and 0.75, as m_{i2} increases, $\sigma_T/\gamma D$ first decreases when $m_{i2}<20$ and then remains constant when $m_{i2}\geq 20$; for $\eta=1.00$, $\sigma_T/\gamma D$ remains constant as m_{i2} increases. These observations illustrate that, for these selected cases, the whole failure will happen at the tunnel face for $\eta=0.00$, 0.25 and 1.00; for $\eta=0.50$ and 0.75, the whole failure will happen when $m_{i2}<20$ and the upper partial failure will occur when $m_{i2}\geq 20$. This indicates that the possibility of upper partial failure at the tunnel face will decreases with η decreases. Also, from Fig. 18(a), one can find that $\sigma_T/\gamma D$ greatly increases as η increases, which can be partially illustrated by the failure surfaces with changing η presented in Fig. 18b.

Finally, the effect of tunnel diameter D on the tunnel face stability with different m_{i2} is provided in Fig. 19. The adopted parameters are as follows: $\eta=0.5$, $GSI_1=10$, $m_{i1}=5$, $\sigma_{ci1}=1$MPa, $GSI_2=10$, $\sigma_{ci2}=2$MPa, and $\gamma_1=\gamma_2=25$kN/m^3. From Fig. 19a, it can be seen that, for these selected cases, the upper partial failure will happen for $D=8$m and $D=10$m when $m_{i2}\geq 20$; for $D=12$m and $D=14$m, the upper partial failure will happen when $m_{i2}\geq 25$. This indicates that the possibility of upper partial failure at the tunnel face will reduce as D increases. Also, from Fig. 19a, one can find that $\sigma_T/\gamma D$ greatly increases as D increases, which can be illustrated by the change of the failure surface from a smaller size to a larger one with D increases (see Fig. 19b).

Tunnel face stability considering seepage forces

To better investigate the tunnel face stability considering the upper partial failure in layered materials, the effect of seepage forces on the tunnel face is conducted in this section. To obtain the seepage forces induced by the tunnel excavation, a numerical model based on FLAC3D is established, as shown in Fig. 20. In Fig. 20, the vertical surfaces of the numerical model and tunnel linings are assumed to be hydraulically impervious, but the tunnel face is pervious. Once the numerical seepage field is obtained, the interpolation tool (griddata)

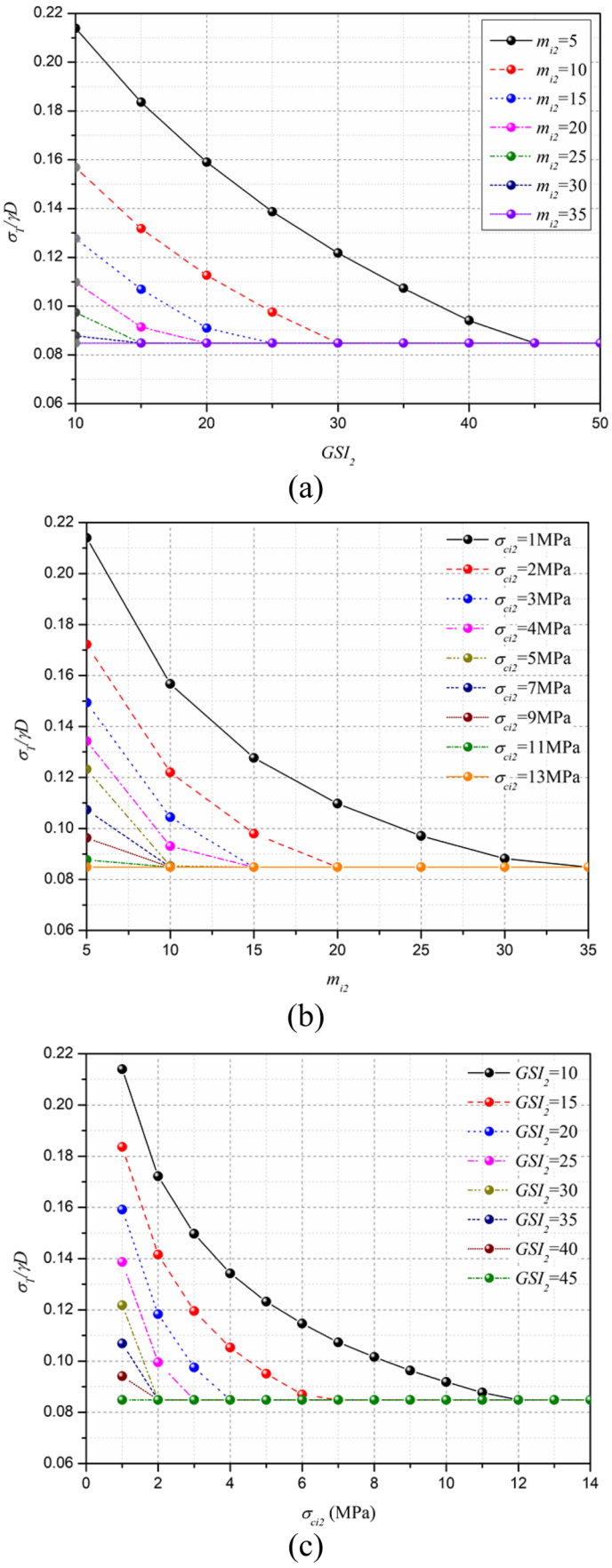

Fig. 16 Normalized limit support pressures with changing rock properties **a** $\sigma_{ci2}=1$MPa; **b** $GSI_2=10$; **c** $m_{i2}=5$

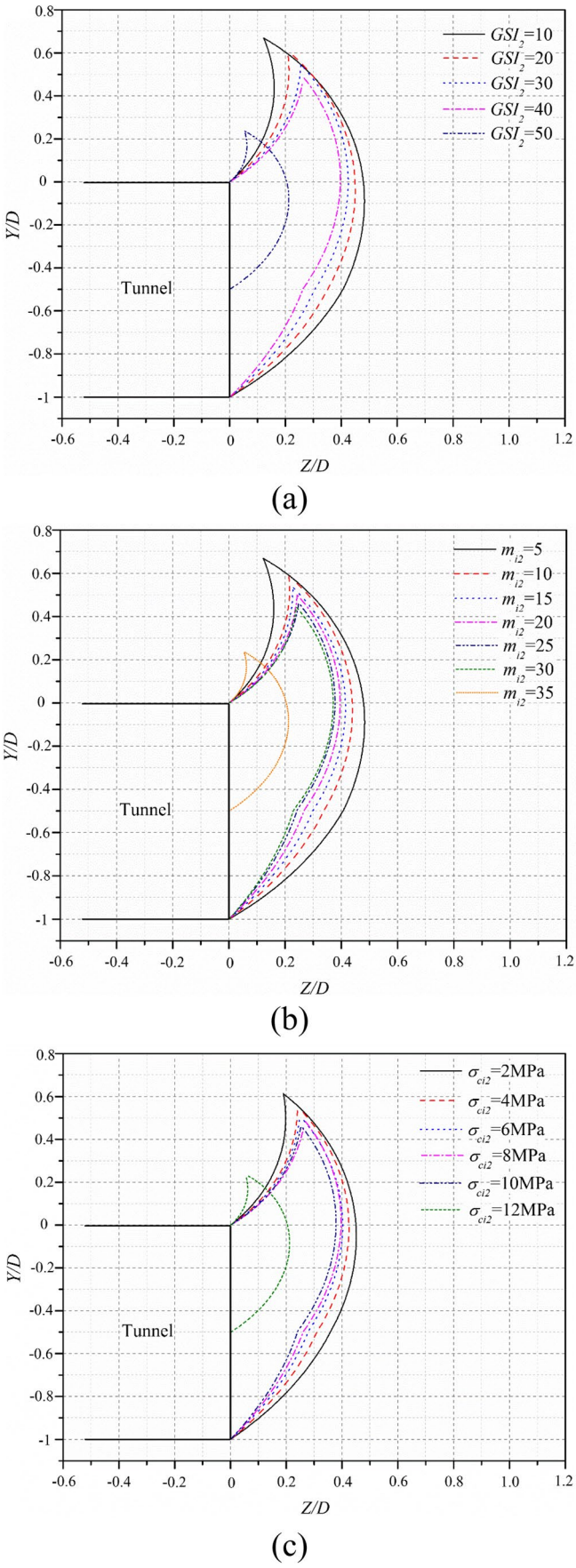

Fig. 17 Failure surfaces with changing rock properties **a** $\sigma_{ci2}=1$MPa and $m_{i2}=5$; **b** $GSI_2=10$ and $\sigma_{ci2}=1$MPa; **c** $m_{i2}=5$ and $GSI_2=10$

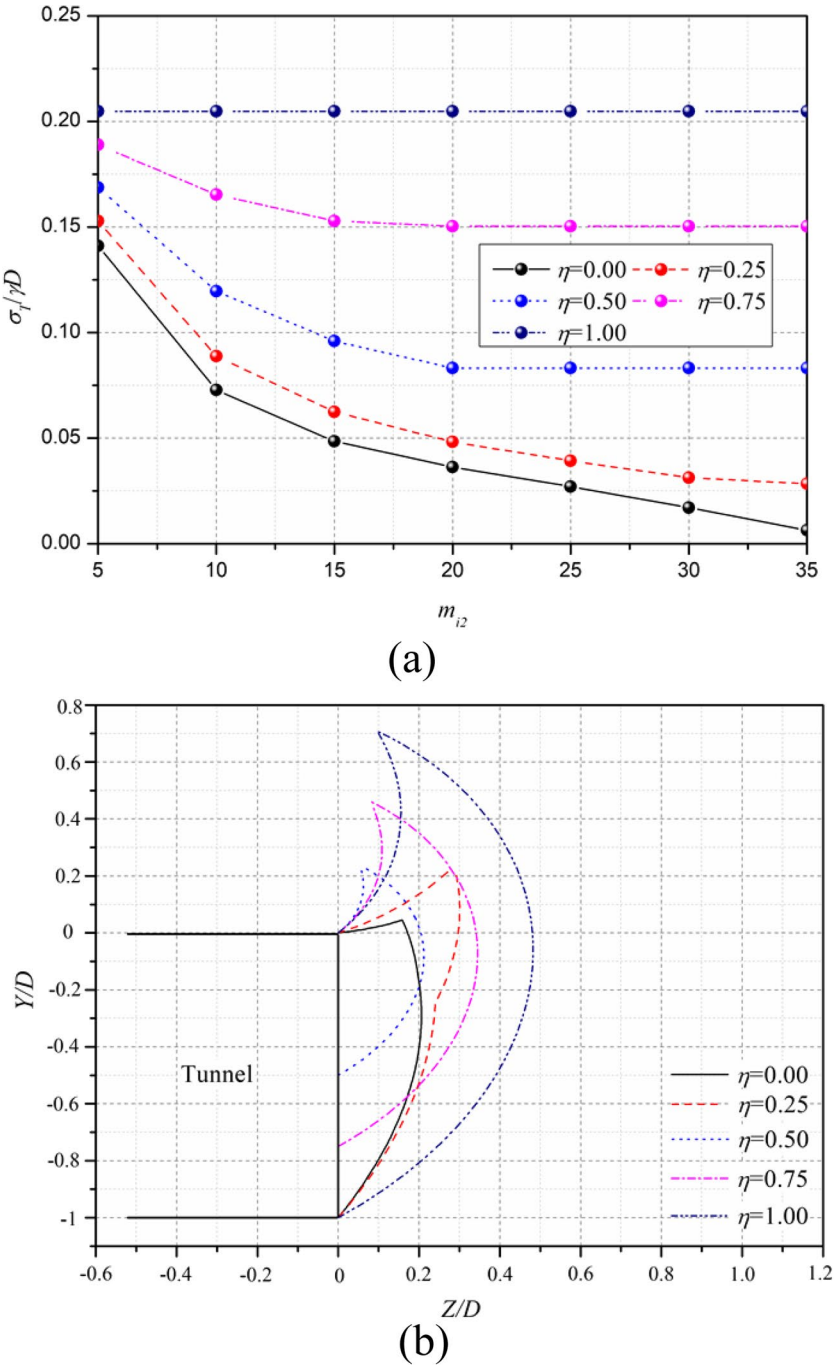

Fig. 18 Effect of η on the tunnel face stability **a** normalized limit support pressures with changing η and m_{i2}; **b** failure surfaces with changing η ($m_{i2}=20$)

in MATLAB is then employed to calculate the interpolated seepage field (see Fig. 21). Note that, in Fig. 21, the seepage forces in the tunnel are set to zero, and only the interpolated seepage field in the study area is provided. Based on the interpolated seepage field, the seepage forces can be more efficiently incorporated into the analytical model to assess the tunnel face stability compared with the traditional method using the numerical seepage field (Pan and Dias 2016b, 2018; Zou et al. 2019b). Referring to Pan and Dias (2016b), the work rate done by the seepage forces can be described as,

$$W_p = -\int_S u \cdot n \cdot v dS = \omega \cdot \sum_{i,j} \left(u_{i,j} \cdot R_{i,j} \cdot S_{i,j} \cdot \sin\left[\varphi_t\right]_{i,j} \right) \tag{29}$$

where $u_{i,j}$ denotes the seepage force in the center of $S_{i,j}$. Combining Eq. (20) and Eq. (22), the limit support pressures

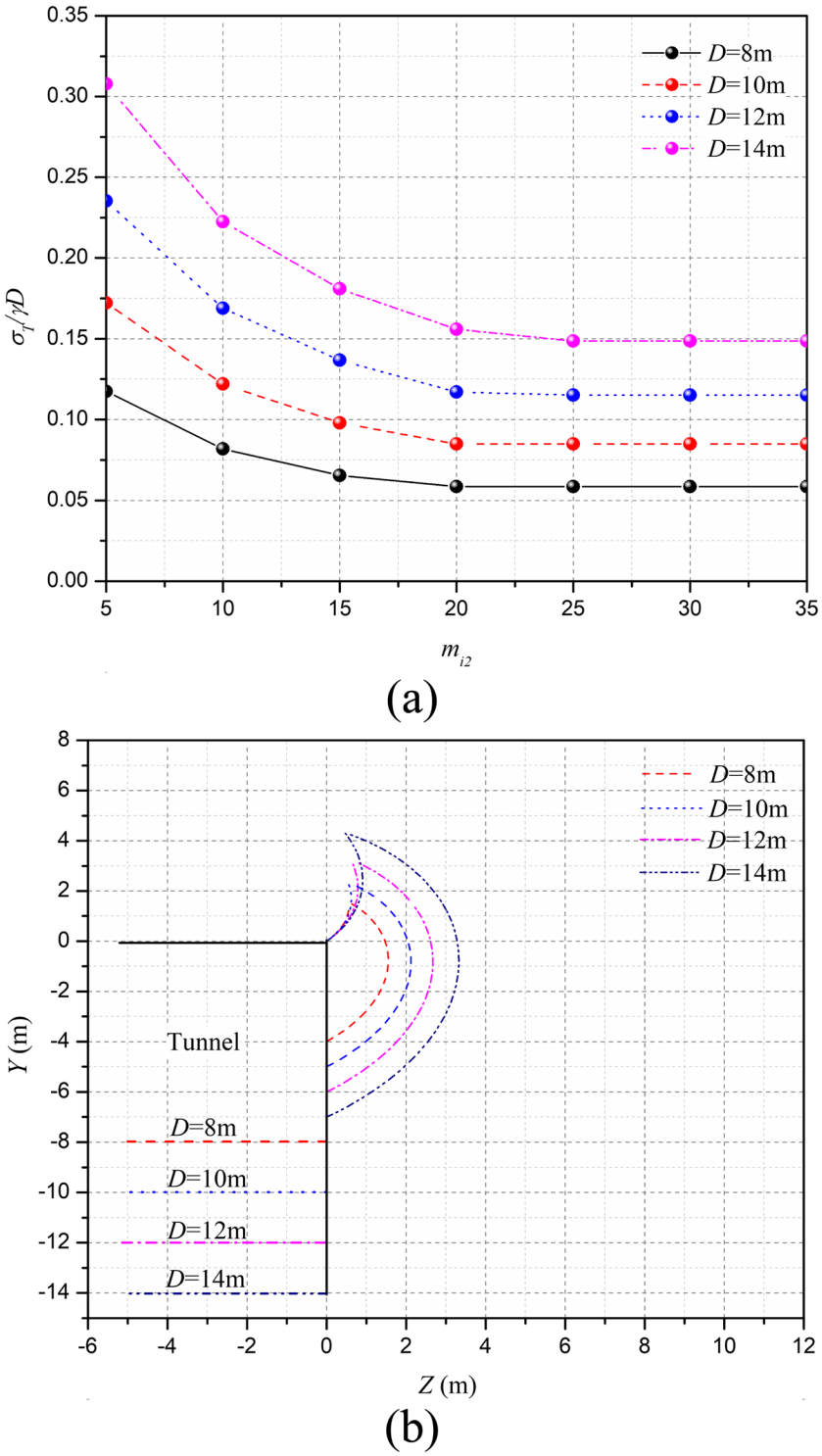

Fig. 19 Effect of D on the tunnel face stability **a** normalized limit support pressures with changing D and m_{i2}; **b** failure surfaces with changing D ($m_{i2}=25$)

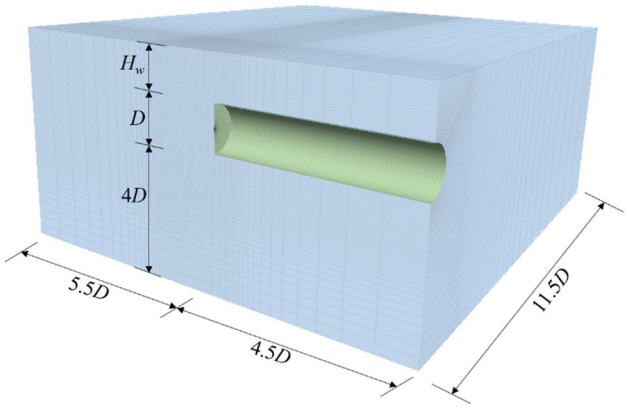

Fig. 20 Numerical model to calculate the seepage field

considering the seepage forces for whole and upper partial failures can then be respectively expressed by,

$$\sigma_{T1} = \max_{(r_E/D,\beta_E,[\varphi_t]_i)} \left(N_\gamma + N_p - N_c\right) \tag{30}$$

$$\sigma_{T2} = \max_{(r_E/D,\beta_E,[\varphi_t]_i,r_t)} \left(N_\gamma + N_p - N_c\right) \tag{31}$$

with

$$N_p = \frac{\sum_{i,j}\left(u_{i,j}\cdot R_{i,j}\cdot S_{i,j}\cdot \sin\left[\varphi_t\right]_{i,j}\right)}{\sum_j\left(R_j\cdot\sum_j\cdot\cos\beta_j\right)} \tag{32}$$

The final limit support pressure considering seepage forces can then be obtained by the maximum of Eq. (30) and Eq. (31).

Figure 22 shows the effect of seepage forces on the tunnel face stability with different m_{i2}. The adopted parameters are as follows: $\eta=0.5$, $GSI_1=10$, $m_{i1}=5$, $\sigma_{ci1}=1$MPa, $\gamma_1=\gamma_2=25$kN/m^3, $GSI_2=10$, and $\sigma_{ci2}=3$MPa. From Fig. 22a, it can be seen that, compared with the case with no seepage forces (see Fig. 16b), the limit support pressure considering seepage forces greatly improves, and the limit support pressure significantly increases as the relative water table H_w/D increases. Also, in Fig. 22a, one can find that, for different H_w/D, the whole failure will happen when $m_{i2}<25$, and the upper partial failure will happen when $m_{i2}\geq 25$. Therefore, combining Fig. 16b, one can conclude that the presence of underground water can delay the occurrence of upper partial failure at the tunnel face. From Fig. 22b, it can be seen that, compared with the case with no seepage forces, the failure surfaces considering seepage forces are much wider, and the magnitude of the failure surface greatly increases as H_w/D increases. This observation is similar to the

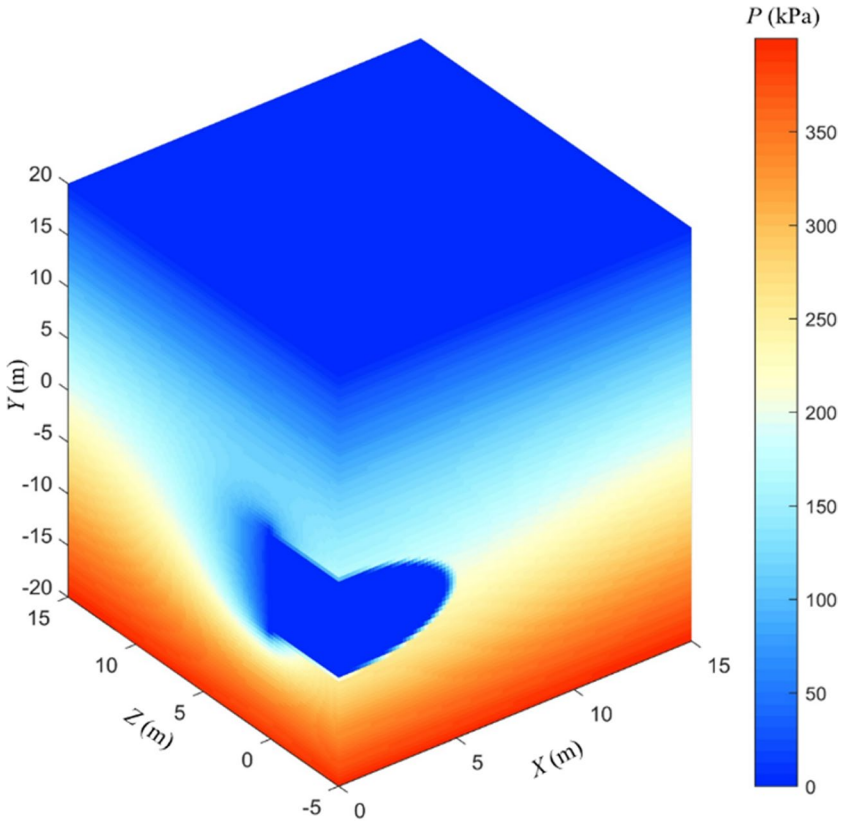

Fig. 21 Interpolated seepage field based on numerical results using the interpolation tool in MATLAB ($H_w/D=2.0$)

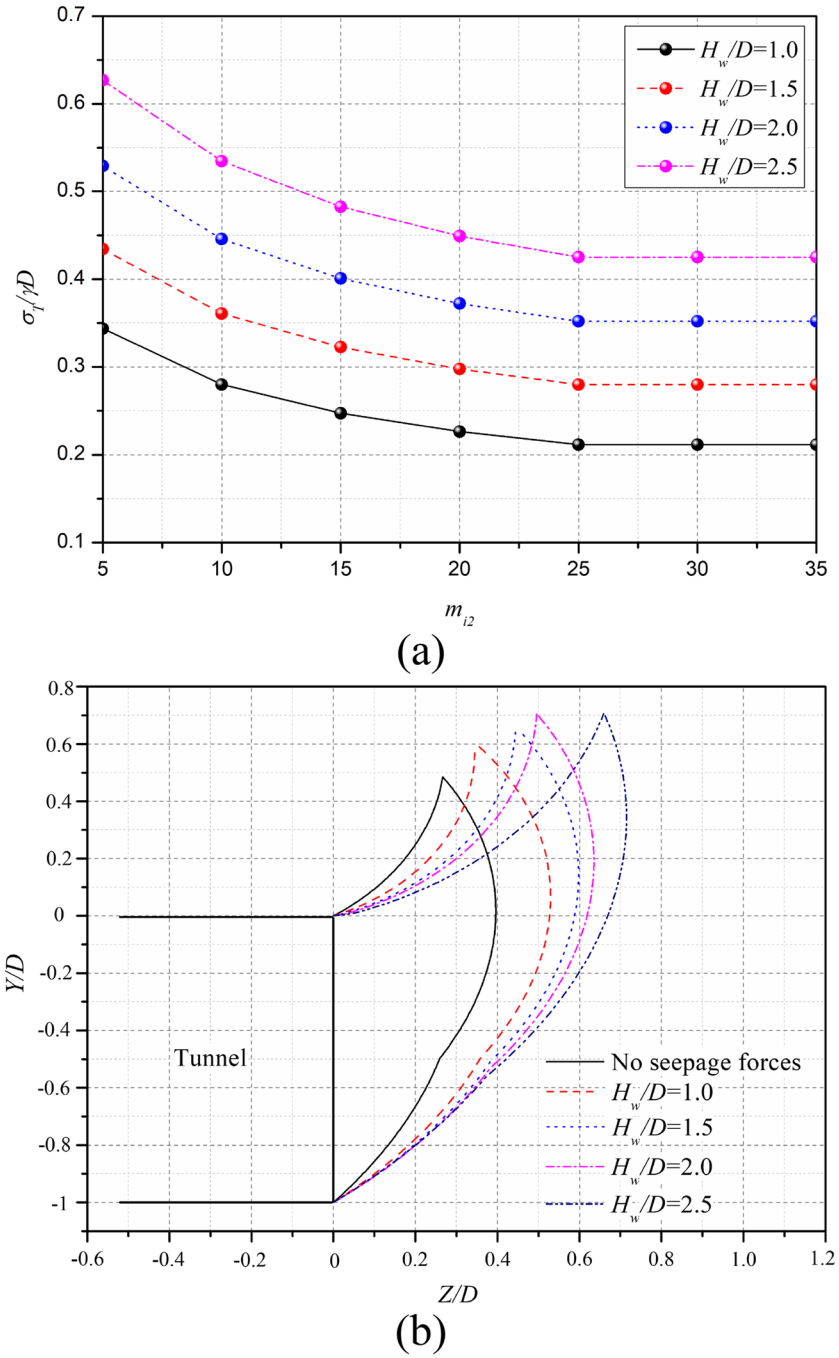

Fig. 22 Effect of seepage forces on the tunnel face stability **a** limit support pressures with changing H_w/D and m_{i2}; **b** failure surfaces with changing H_w/D ($m_{i2}=20$)

result obtained by Di et al. (2023c) in homogeneous soils. This can be used to partially illustrate the increase of the limit support pressure with the increasing of H_w/D.

Conclusions

In this study, an effective approach is proposed to assess the tunnel face stability with considering the possibility of the upper partial failure at the tunnel face in layered rock masses. Compared with previous works, the following improvements are achieved.

(1) To incorporate the properties of layered rock masses into the stability analysis of the tunnel face, a multi-tangent method is introduced and adopted to calculate the equivalent Mohr–Coulomb parameters. The influence of number of tangential lines k on the stability issue is conducted, and the results show that $k=3$ is the best choice for these selected cases, which ensures

the computational efficiency and satisfies the accuracy of results.

(2) Validations of the proposed method by comparing with published analytical solutions and numerical results are conducted, showing that the proposed method is an accurate and effective approach to assess the tunnel face stability under different types of failure (whole failure or upper partial failure) in layered materials.

(3) Based on the proposed method, the effects of rock properties, layered position and tunnel diameter on the tunnel face stability are presented. It is shown that, when a soft material in the upper section of tunnel face, the upper partial failure is likely to happen and this possibility will increase as the properties of lower layer increase, the tunnel diameter decreases and the layered position moves down. The properties of lower layer have strong influence on the stability issue when whole failure happens at the tunnel face. For cases of whole failure or upper partial failure, a larger limit support pressure is associated to a larger failure surface.

(4) With the aid of numerical simulation, the effect of seepage forces is also incorporated into the stability analysis of tunnel faces. The results show that the limit support pressure and the magnitude of failure surface greatly increases under seepage forces, and the presence of underground water delays the occurrence of upper partial failure at the tunnel face.

Author contribution Conceptualization: Guang-Hui Chen, Jin-Feng Zou. Formal analysis: Guang-Hui Chen. Methodology: Guang-Hui Chen, Jin-Feng Zou. Project administration: Jin-Feng Zou. Resources: Guang-Hui Chen, Jin-Feng Zou. Validation: Guang-Hui Chen. Writing—original draft: Guang-Hui Chen, Jin-Feng Zou. Writing—review and editing: Guang-Hui Chen.

Funding The support from the Guizhou Provincial Science and Technology Major Project (Qian-ke-he-zhong-da-zhuan-xiang-zi [2018]3010) is greatly appreciated.

Data availability All data, models, or code generated or used during the study are available from the corresponding author by request.

Declarations

Competing interests The authors declare no competing interests.

References

Alagha AS, Chapman DN (2019) Numerical modelling of tunnel face stability in homogeneous and layered soft ground. Tunn Undergr Space Technol 94:103096

Chen Y, Lin H (2019) Consistency analysis of Hoek-Brown and equivalent Mohr-coulomb parameters in calculating slope safety factor. Bull Eng Geol Env 78(6):4349–4361

Chen GH, Zou JF, Xiang XY, Pan QJ, Qian ZH (2021) Stability assessments of reinforced tunnel face using improved homogenization approach. Int J Geomech 21(10):04021183

Chen GH, Zou JF, Yang T, Shi HY (2022) Three-dimensional modified pseudo-dynamic analysis of reinforced slopes with inclined soil nails. Bull Eng Geol Env 81(9):377

Chen GH, Zou JF, Wei XX, Guo QF (2023) Three-dimensional blow-out stability analysis of shield tunnel face in anisotropic and heterogeneous soils. Tunn Undergr Space Technol 131:104851

Chen G, Zou J, Qian Z (2022) Analysis of tunnel face stability with non-linear failure criterion under the pore water pressure. Eur J Environ Civ Eng 26(7):2950–2962

Cheng H, Chen J, Chen R, Huang J, Li J (2019) Three-dimensional analysis of tunnel face stability in spatially variable soils. Comput Geotech 111:76–88

Di Q, Li P, Zhang M, Cui X (2023a) Experimental investigation of face instability for tunnels in sandy cobble strata. Underground Space 10:199–216

Di Q, Li P, Zhang M, Cui X (2023b) Experimental study of face stability for shield tunnels in sandy cobble strata of different densities. Tunn Undergr Space Technol 135:105029

Di Q, Li P, Zhang M, Wu J (2023c) Influence of permeability anisotropy of seepage flow on the tunnel face stability. Underground Space 8:1–14

Dias D, Janin JP, Soubra AH, Kastner R (2008) Three-dimensional face stability analysis of circular tunnels by numerical simulations. In GeoCongress 2008: Characterization, Monitoring, and Modeling of GeoSystems 886–893

Ding W, Liu K, Shi P, Li M, Hou M (2019) Face stability analysis of shallow circular tunnels driven by a pressurized shield in purely cohesive soils under undrained conditions. Comput Geotech 107:110–127

Han K, Wang L, Su D, Hong C, Chen X, Lin XT (2021) An analytical model for face stability of tunnels traversing the fault fracture zone with high hydraulic pressure. Comput Geotech 140:104467

Hoek E, Diederichs MS (2006) Empirical estimation of rock mass modulus. Int J Rock Mech Min Sci 43(2):203–215

Hoek E, Carranza-Torres C, Corkum B (2002) Hoek-Brown failure criterion-2002 edition. Proc NARMS-Tac 1(1):267–273

Hou C, Zhang Z, Yang X (2022) Three-dimensional tunnel face stability considering the steady-state seepage in saturated and unsaturated regions with changing water levels. Comput Geotech 146:104741

Ibrahim E, Soubra AH, Mollon G, Raphael W, Dias D, Reda A (2015) Three-dimensional face stability analysis of pressurized tunnels driven in a multilayered purely frictional medium. Tunn Undergr Space Technol 49:18–34

Jafari P, Fahimifar A (2022) Upper-bound face stability analysis of rectangular shield-driven tunnels in undrained clays. Comput Geotech 146:104739

Jin D, Zhang Z, Yuan D (2021) Effect of dynamic cutterhead on face stability in EPB shield tunneling. Tunn Undergr Space Technol 110:103827

Li Y, Emeriault F, Kastner R, Zhang ZX (2009) Stability analysis of large slurry shield-driven tunnel in soft clay. Tunn Undergr Space Technol 24:472–481

Li T, Pan Q, Shen Z, Gong W (2022) Probabilistic stability analysis of a tunnel face in spatially random Hoek-Brown rock masses with a multi-tangent method. Rock Mech Rock Eng 55(6):3545–3561

Liu W, Wu B, Shi P, Xu X (2021) Analysis on face stability of rectangular cross-sectional shield tunneling based on an improved two-dimensional rotational mechanism. Acta Geotech 16(11):3725–3738

Liu W, Shi P, Yu M, Jia P (2022) Analysis of working face stability during obstruction removal from a box tunnel machine. Acta Geotech 17(10):4627–4639

Lü X, Zhou Y, Huang M, Zeng S (2018) Experimental study of the face stability of shield tunnel in sands under seepage condition. Tunn Undergr Space Technol 74:195–205

Maleki M, Imani M (2022) Active lateral pressure to rigid retaining walls in the presence of an adjacent rock mass. Arab J Geosci 15(2):1–11

Man J, Huang H, Ai Z, Chen J (2022b) Analytical model for tunnel face stability in longitudinally inclined layered rock masses with weak interlayer. Comput Geotech 143:104608

Man J, Zhou M, Zhang D, Huang H, Chen J (2022a) Face stability analysis of circular tunnels in layered rock masses using the upper bound theorem. J Rock Mech Geotech Eng 14(6):1836–1848

Mao N, Al-Bittar T, Soubra AH (2012) Probabilistic analysis and design of strip foundations resting on rocks obeying Hoek-Brown failure criterion. Int J Rock Mech Min Sci 49:45–58

Meng F, Chen R, Mooney MA, Wu H, Jia Q (2022) Evaluation of shield tunneling-induced soil disturbance in typical structured clays. Bull Eng Geol Env 81(4):1–16

Mollon G, Dias D, Soubra AH (2011) Rotational failure mechanisms for the face stability analysis of tunnels driven by a pressurized shield. Int J Numer Anal Meth Geomech 35(12):1363–1388

Pan Q, Dias D (2016a) Face stability analysis for a shield-driven tunnel in anisotropic and nonhomogeneous soils by the kinematical approach. Int J Geomech 16(3):04015076

Pan Q, Dias D (2016b) The effect of pore water pressure on tunnel face stability. Int J Numer Anal Meth Geomech 40(15):2123–2136

Pan Q, Dias D (2018) Three dimensional face stability of a tunnel in weak rock masses subjected to seepage forces. Tunn Undergr Space Technol 71:555–566

Qian Z, Zou J, Pan Q, Dias D (2019) Safety factor calculations of a tunnel face reinforced with umbrella pipes: a comparison analysis. Eng Struct 199:109639

Qin C, Chian SC (2018) Seismic ultimate bearing capacity of a Hoek-Brown rock slope using discretization-based kinematic analysis and pseudodynamic methods. Int J Geomech 18(6):04018054

Saada Z, Maghous S, Garnier D (2013) Pseudo-static analysis of tunnel face stability using the generalized Hoek-Brown strength criterion. Int J Numer Anal Meth Geomech 37(18):3194–3212

Seghateh Mojtahedi A, Imani M, Fahimifar A (2021) Three-dimensional face stability analysis of deep and shallow tunnels in rock masses. Int J Geomech 21(10):04021193

Senent S, Jimenez R (2015) A tunnel face failure mechanism for layered ground, considering the possibility of partial collapse. Tunn Undergr Space Technol 47:182–192

Senent S, Mollon G, Jimenez R (2013) Tunnel face stability in heavily fractured rock masses that follow the Hoek-Brown failure criterion. Int J Rock Mech Min Sci 60:440–451

Shen J, Priest SD, Karakus M (2012) Determination of Mohr-Coulomb shear strength parameters from generalized Hoek-Brown criterion for slope stability analysis. Rock Mech Rock Eng 45(1):123–129

Vásárhelyi B (2009) A possible method for estimating the Poisson's rate values of the rock masses. Acta Geodaet Geophys Hung 44(3):313–322

Wang FY, Zhou ML, Zhang DM, Huang HW, Chapman D (2019) Random evolution of multiple cracks and associated mechanical behaviors of segmental tunnel linings using a multiscale modeling method. Tunn Undergr Space Technol 90:220–230

Wang J, Lin G, Xu G, Wei Y, Li S, Tang X, He C (2022) Face stability of EPB shield tunnels in multilayered ground with soft sand lying on hard rock considering dynamic excavation process: a DEM study. Tunn Undergr Space Technol 120:104268

Weng X, Sun Y, Yan B, Niu H, Lin R, Zhou S (2020) Centrifuge testing and numerical modeling of tunnel face stability considering longitudinal slope angle and steady state seepage in soft clay. Tunn Undergr Space Technol 101:103406

Wu W, Liu X, Guo J, Sun F, Huang X, Zhu Z (2021) Upper limit analysis of stability of the water-resistant rock mass of a Karst tunnel face considering the seepage force. Bull Eng Geol Env 80(7):5813–5830

Xu J, Du X (2023) Seismic stability of 3D rock slopes based on a multi-cone failure mechanism. Rock Mech Rock Eng 56(2):1595–1605

Yang XL, Li L, Yin JH (2004) Seismic and static stability analysis for rock slopes by a kinematical approach. Geotechnique 54(8):543–549

Yin X, Chen R, Meng F (2021) Influence of seepage and tunnel face opening on face support pressure of EPB shield. Comput Geotech 135:104198

Zhang C, Han K, Zhang D (2015) Face stability analysis of shallow circular tunnels in cohesive-frictional soils. Tunn Undergr Space Technol 50:345–357

Zhang R, Chen G, Zou J, Zhao L, Jiang C (2019) Study on roof collapse of deep circular cavities in jointed rock masses using adaptive finite element limit analysis. Comput Geotech 111:42–55

Zhang M, Di Q, Li P, Wei Y, Wang F (2022) Influence of non-associated flow rule on face stability for tunnels in cohesive-frictional soils. Tunn Undergr Space Technol 121:104320

Zhao LH, Cheng X, Li L, Chen JQ, Zhang Y (2017) Seismic displacement along a log-spiral failure surface with crack using rock Hoek-Brown failure criterion. Soil Dyn Earthq Eng 99:74–85

Zhou J, Qin C (2022) Prediction of limit support pressure for face stability of deep tunnels buried beneath sea/water. Eur J Environ Civ Eng 26(11):5012–5030

Zou J, Chen G, Qian Z (2019a) Tunnel face stability in cohesion-frictional soils considering the soil arching effect by improved failure models. Comput Geotech 106:1–17

Zou JF, Qian ZH, Xiang XH, Chen GH (2019b) Face stability of a tunnel excavated in saturated nonhomogeneous soils. Tunn Undergr Space Technol 83:1–17